Design and Evaluation of Simulated PEM Scanner for Early-Stage Breast Lesion Detection

By

Bethel Haile Tekleyohannis

In partial fulfilment of the Requirements for the Degree of Master of Science in Biomedical Engineering

Centre of Biomedical Engineering

Addis Ababa Institute of Technology

Advisor: Dawit Assefa Haile (PhD)

Co-Advisor: Mr. Samuel Taddesse Abebe (MSc)

Jan 2022

Addis Ababa, Ethiopia

Declaration

I declare that all information in this document has been obtained and presented based on the required academic rules and ethical conduct. As required by these rules and conducts, I have fully cited and referenced all materials and results that are not original to this work.

Name: Bethel Haile Tekleyohannis _____

Signature: _____

Date: _____

This MSc. thesis has been submitted for examination with my approval as an advisor.

_____

Dawit Assefa Haile (PhD)

_____

Samuel Taddesse Abebe (MSc)

Certificate of Examination

This is to certify that the thesis prepared by Bethel Haile Tekleyohannis entitled "**Design and Evaluation of Simulated PEM Scanner for Early-Stage Breast Lesion Detection"** submitted in partial fulfilment of the requirements for degree of Master of Science in Biomedical Engineering (Bioinstrumentation and Imaging) complies with the regulations of the University and meets the accepted standards with respect to originality and quality.

Signed by the Examining Committee

External Examiner	Signature	Date
Internal Examiner	Signature	Date
Dr. Dawit Assefa Haile Advisor	Signature	Date

Chief of Department or Graduate Program Coordinator

ACKNOWLEGMENTS

First and foremost, I express my earnest appreciation to my humble advisor Dr. Dawit Assefa Haile (PhD) and my Co-Advisor Mr. Samuel Taddesse Abebe (MSc), for their support and guidance. Especially my co-advisor has countless role in this thesis in providing me with all the required skills and research tools to complete this research. In addition, my gratitude goes to staffs at the Centre of Biomedical Engineering, Addis Ababa Institute of Technology, AAU for helping me through my academic journey. To my parents, Haile Tekleyohannis and Belaynesh Kassaye, words alone cannot express how grateful I am for the support you gave me in my entire life. Thanks for your great Love. Finally, I would like to thank the University of Gondar for the chance of this scholarship.

ABSTRACT

Breast cancer is the most commonly diagnosed cancer in females worldwide, contributing around 11.7 % (~2.3 million people) of new cancer cases in 2020 only, with a death rate of 6.9%. Early diagnosis and check-up are essential for effective treatment and reduction of incidences and mortality rates. Different modalities exist to diagnose breast cancers. Positron emission tomography (PET) is the one imaging tool in nuclear medicine providing physiological information about the breast by quantifying the metabolic activities of the cells in the breast tissues. Both whole-body (WB) PET scanners and organ-specific PET scanners are available in the market. But current trends show that there is a complete shift towards dedicated, organ specific PETs. One of those is Positron Emission Mammography (PEM), believed to be better than mammography and other imaging modalities to detect small breast lesions. Semiconductor-based PEM detectors are simulated with good spatial resolution but are expensive. Scintillator-based PET and PEM detectors can provide quit good sensitivity and are cost effective. On the contrary, these detectors cannot detect small breast lesions due to their poor spatial resolution. This requires development of detectors that give rise to better spatial resolution. In the current thesis work, a high-performance PEM scanner is simulated using TOC (Transparent Optical Ceramic) scintillators of 1 x 1 x 10mm^3 crystals with the aim to improve the spatial resolution, sensitivity as well as scattering fraction. Those TOC scintillators are LHO: cerium doped lutetium hafnate (Lu_2 Hf_2 O_7: Ce), BHO: cerium doped barium hafnate ($BaHfO_3$: Ce) and SHO: cerium doped strontium hafnate ($SrHfo_3$: Ce). The design was based on the GATE (Geant4 Application for Emission Tomography) simulation software. Its performance was tested and evaluated by following the NEMA (National Electrical Manufacturers Association) NU 4-2008 standards. The complete scanner has 39 heads and 10 x 30 x 59 modules in the detector. Based on the type of scintillator used, the designed scanner provided a spatial resolution between 1.0 and 1.1 mm FWHM (Full Width at Half Maximum) in the axial direction, 7.24% to 9.11% system sensitivity and 11.01% to 11.19% scatter fraction. The design offered good uniformity as well as image quality. The computed spatial resolution, sensitivity and scatter fraction values are superior to those already reported in the literature.

Key words: Breast Cancer, GATE, PEM, PET, Semiconductor, Scintillator, TOCs, NEMA standard.

TABLE OF CONTENT

Contents

LIST OF TABLES

LIST OF FIGURES

ABBREVIATIONS

1D	One Dimensional
2D	Two Dimensional
3D	Three Dimensional
APD	Avalanche Photo Diodes
BGO	Bismuth Germanate
BHO	Cerium-doped Barium Hafnate ($BaHfO_3$: Ce)
Br	Bromine
C	Carbon
CdTe	Cadmium Telluride
CFOV	Centre Field of View
CNR:	Contrast-to-Noise-Ratio
CT	Computed Tomography
CZT	Cadmium Zinc Telluride
DC	Direct Current
DOI	Depth of Interaction
LHO	Cerium-doped Lutetium Hafnate ($Lu_2Hf_2O_7$: Ce)
F	Florien
FBP	Filtered Back Projection
FOV	Field of View
FT	Fourier Transform
FWHM	Full Width at Half Maximum
FWTM	Full Width at Tenth Maximum
GATE	Geant4 Application for Emission Tomography
Ge	Germanium
GSO	Gadolinium Oxy-Silicate
I	Iodine
keV	Kiloelectron Volt
LIOB	Laser Induced Optical Barrier
LM-OSEM	List Mode-Ordered Subset Expectation Maximization
LOR	Line of Response

LSO	Lutetium Oxyorthosilicate
LuAP	Lutetium Aluminum Perovskite
LYSO	Lutetium Yttrium Oxyorthosilicate
MC-PMT	Multi-Channel-Photo Multiplier Tube
MLEM	Maximum Likelihood Expectation Maximization
MRI	Magnetic Resonance Imaging
N	Nitrogen
NaI	Sodium Iodide
NEMA	National Electrical Manufacturers Association
O	Oxygen
OE	Origin Ensemble
OSEM	Ordered Subset Expectation Maximization
PET	Positron Emission Tomography
PEM	Positron Emission Mammography
PMT	Photo Multiplier Tube
PSF	Point Spread Function
PS-PMT	Position Sensitive-Photo Multiplier Tube
RAMLA	Raw Action Maximum Likelihood Algorithm
RC	Recovery Co-efficient
SF	Scatter Fraction
SHO	Cerium Doped Strontium Hafnate ($SrHfo_3$: Ce)
Si	Silicon
SiPMs	Silicon Photo Multipliers
SNR	Signal-to-Noise- Ratio
SPECT	Single Photon Emission Computed Tomography
SR	Spatial Resolution
TOC	Optical Transparent Ceramic
TOF	Time of Flight
USPAP	United States Patent Application Publication
UV	Ultraviolet
WB	Whole Body

CHAPTER ONE

INTRODUCTION

1.1. Background

Breast cancer is a common type of cancer in women being one of the main causes of death. Men can also develop breast cancers but the incidence is very rare. About 90% of breast cancer cases start in the milk ducts or lobules that supply milk to the duct [1] It is the most commonly diagnosed cancer in females worldwide, contributing to 11.7 % (~ 2.3 million people) new cancer cases in 2020 only, with a death rate of 6.9% [2]. For comparison, there were nearly 246,660 new cases in 2017 and with more than 40,000 deaths [3]. In Africa, 168,690 cases and 74,072 deaths occurred in 2018. Nigeria was the leading country with 26,310 cases and 11, 564 deaths followed by Egypt with 9,254 deaths out of a total of 23,081 new cases [4]. In Ethiopia, 9,061 deaths and 16,133 new cases were recorded in 2020 [5]. This made breast cancer the most spread out and larger in number compared with other cancer types in the country [5]. Early diagnosis is widely approved as being essential for effective treatment as well as reducing the incidences and mortality rates.

There are different modalities that exist to diagnose breast cancers. Positron emission tomography (PET) is the one imaging tool in nuclear medicine providing physiological information about the breast by quantifying the metabolic activities of the cells in the breast tissues [6]. PET uses a special tracer that contains a radioactive tracer or radioactive isotope produced by an accelerator called a cyclotron [7]. The cyclotron accelerates charged particles to a magnetic field. The radiotracer is inhaled, swallowed, or injected into the patient's arm an hour before a PET scan depending on the part of the body being examined. Certain normal organs/tissues absorb the tracer. But most of the time, it is the abnormal cells/tissues/organs that would absorb the tracer. The tracer is mostly concentrated in areas of higher chemical activity. Abnormal organs, tissues, and cells with high chemical activities could be detected during a PET scan. PET scans can measure blood flow, metabolism (oxygen use) and body sugar use. In the USA only, around 2 million PET scans are performed annually showing their tremendous uses in various clinics. Of course, a PET scan is used not only to detect breast cancers but also other heart problems, brain disorders and other diseases in the central nervous system.

Both whole-body (WB) PET scanners as well as those that are organ-specific PET scanners are available in the market. But current trends show that there is a complete shift towards dedicated, organ-specific PETs. One of those is Positron Emission Mammography (PEM). In WB PET imaging, the detector exposes all parts of the body then stitches together the different sections to present a whole-body image. The problem behind this approach is that different parts of the body are scanned at different times and the radioactive tracers are distributed in the body at different times. That is to mean the bio-distribution of the tracers differs in different organs [8]. For solving this problem, organ-specific radiotracers are being introduced. WB PET has drawbacks in terms of resolution, scanning time, sensitivity, and image quality. An increase in sensitivity comes with an increase in the scatter fraction along with the requirement for a data-acquisition system [9]. The key factors for the PET performance are the detector elements which are characterized by timing, stopping power, quantum efficiency, energy resolution, and cost-effectiveness [3].

PEM is a breast-dedicated imaging device that uses a pair of annihilation gamma photons to detect abnormalities in the breast tissues. It comes with a better spatial resolution compared to WB PET. There are still various efforts to improve the spatial resolution and sensitivity of PEM scanners. Besides, PEM devices are usually compact with a limited field of view to cover the full breast area. In order to successfully diagnose breast cancers at early stages, a device with good geometrical design to cover full breast area, high sensitivity and high spatial resolution is required [3]. The image resolution as well as the field of view mostly depend on the quality of the detectors used. Semiconductor material-based PEM detectors are proved to have an excellent spatial resolution. But those are expensive. Whereas scintillator crystals-based detectors are cost-effective but have limitations on their intrinsic resolution to identify small breast lesions. The annihilation phenomenon is the basis for PET/M imaging [7]. Annihilation is the event that is produced when a positron interacts with an ordinary electron in the surrounding matter. Positrons travel only a short distance before colliding with electrons. The annihilation event generates paired 511-KeV photons which are detected by the PET detector. The paired photons travel in opposite directions 180 degrees apart. Different types of events, called coincidences could happen following the emission of photons. The whole event is captured by a gamma camera

where the data is reconstructed in a manner similar to in single-photon emission computed tomography (SPECT).

There are some important considerations in PET/PEM imaging. The first one is the spatial resolution that dictates the ability of the imaging modality to provide detailed information about the object being scanned [8]. Sensitivity is another one that is determined by the absorption efficiency of the detector system and its solid angle of coverage of the image [10]. Others include scattering fraction, image quality and uniformity, which are much related to the sensitivity and spatial resolution. In that regard, there are still ongoing researches being carried out to improve the resolution, sensitivity, scattering fraction, image quality and uniformity of PEM detectors to come up with organ-specific imaging options. Generally, the performance of a PEM system could be improved in either of three ways: by selecting the best scintillation crystals, selecting the best geometry of known scintillators, or improving the image reconstruction technique. This thesis work intends to design a PEM detector based on existing scintillation crystals with excellent material property and tries to propose an optimal geometry with an aim to enhance the resolution as well as the sensitivity of PEM scanners. Furthermore, recently proposed reconstruction techniques will be utilized to enhance the overall image quality of the PEM scanner. The design work follows procedures that have already been well established in the literature. Accordingly, the simulation has been done on GATE software and its performance has been evaluated based on NEMA NU 4-2008 standards.

1.2. Problem Statement

Breast cancer is the most commonly diagnosed cancer in females worldwide, contributing to 11.7 % (~2.3 million people) of new cancer cases in 2020 only, with a death rate of 6.9% [2]. Early diagnosis is widely approved as being essential for effective treatment and it also helps to reduce the incidences and mortality rates. WB PET scanners do not offer clear information for specific organs. The cause is their far-field of view, poor resolution, and large solid angle (less sensitivity). That was why it has been difficult to diagnose breast cancers on WB PET scanners. Breast cancer detection needs an imaging system that provides better image quality, and PEM is undoubtedly a good alternative. Semiconductor material-based PEM detectors proved an excellent spatial resolution but those are expensive. Scintillator crystals-based

detectors are cost-effective but have limitations on their intrinsic resolution to identify small breast lesions. In that regard, researchers are still trying to come up with detectors with high efficiency, fast response time (more sensitive) and high resolution. And also, to design and implement a high-performance PEM scanner, the scintillator material should have good stopping power, high efficiency, and high light output. Designing a detector system with geometric setup that give rise to such output qualities is then quite important.

1.3. Objective

1.3.1. General Objective

To design and evaluate a high-performance simulated PEM scanner to improve breast abnormality detection.

1.3.2. Specific Objectives

- ✓ Investigate best scintillation crystal material for PEM detector simulation;
- ✓ To design best geometrical set up for the proposed PEM detector;
- ✓ Design the PEM detector based on the GATE software.
- ✓ Evaluate detector's performance based on the NEMA NU 4-2008 standards.
- ✓ Compare the performance of the proposed detector against other detectors proposed in the literature based on qualitative (visual comparison) and/or quantitative measures.

1.4. Scope and Limitations of the Study

This research is a simulation study that involves design and simulation work implemented in-silico. Prolonged evaluations for practical implementation are needed. The design and performance evaluation follow NEMA NU4 2008 guideline standard procedures. To compute the scattering fraction, the phantom size used during evaluation was approximated to fit that of the NEMA NU4 2008 standard.

1.5. Significance of the Study

The proposed design is aimed to design a high-performance PEM detector that enables detecting breast cancers in their early stages. The design was based on scintillators which are cost-effective than using other semi-conductor materials.

1.6. Thesis Organization

The rest of the thesis has been organized into five chapters. Chapter two presents the literature review and important basics on detectors including cerium doped alkaline earth hafnium oxide scintillators. Chapter three deals overview on PET and PEM imaging principles including the state of the art and related image reconstruction mechanisms. In Chapter four the proposed system design, specifications and simulation are discussed. Chapter five presents the results including important discussions. Finally, the conclusion and recommendations of the research work are presented in Chapter six.

CHAPTER TWO

LITERATURE REVIEW

Musa et al. proposed a simulation of high-performance, PEM scanner by using LSO [3]. The PEM detector in their study was a silicon photomultiplier that detects small breast lesions due to its resolution power. The design offered excellent spatial resolution but was not cost-effective. The simulation was done using the GATE software and the performance evaluation test was done based on NEMA standards. The design offered 1.0 mm spatial resolution at the centre of the field of view (CFOV), 2.1mm on the Trans axial direction at 2.5cm axial position, with system sensitivity at 10.6% [3].

The institute of higher energy Physics at Chinese Academy of Sciences studied and developed the polygon positron emission mammography (PEMi) [8]. The design had a polygon structure and was made using lutetium-ytterium orthosilicate (LYSO) crystal arrays mounted on a position-sensitive photomultiplier. The PEMi design resulted in intrinsic spatial resolution of 1.67 mm in axial direction and a tangential resolution which was around 2.5 mm within a 5cm diameter FOV. In a coincidence timing window of 6ns and a 360-660 keV energy window, peak sensitivity measured 6.88%. The resolution of the reconstructed images by PEMi was superior to what could be achieved by WB PET, reducing the lower threshold on detectable lesion size. A clinical trial made by the authors demonstrated that PEMi is clinically feasible [8].

Ekaterina et al. presented a simulation of a brain PET scanner based on a highly pixilated CdTe detector [11]. The simulation and evaluation criteria followed NEMA NU 2-2008 and NEMA NU 4- 2008 standards. Accordingly, the authors obtained a resolution of around 1mm full width at half maximum in all directions. The major issue was the CdTe detector is quite expensive.

Karimiana et al. proposed a Cylindrical Breast PET (CYBPET) system for breast imaging with patients in the prone position. Each breast is scanned separately. The rest of the body and chest are covered by thin plastic to reduce presser fixation and surrounded by a crystal scintillator in the CYBPET ring. The spatial resolution of the CYBPET was 25% better than the WB-PET scanner. The noise-effective count rate (NECR) of CYBPET was about twice that of the WB-PET scanner [12].

Li et al. developed a high-resolution PET camera for brain and breast studies. The design had 21 cm axial length and 54 cm outside diameter [13]. This camera was built by using a pixelated Bismuth Germanate (BGO) detector of crystal dimension 2.7 × 2.7 × 18 mm^3. The camera sensitivity was 9.2% and the resolution was 2.7 mm at CFOV of trans-axial image resolution and 4.0 mm at 10 cm away from the CFOV of the camera.

Karp et al. developed G-PET scanner. The design was high-resolution and high sensitivity brain PET scanner. The system was based on pixelated Gadolinium Oxy-Silicate (GSO) detector with crystal size 4 × 4 ×10 mm^3 and detector size of 42.0 cm x 30.0 cm x 25.6 cm on outside, inside and axial length, respectively. The scanner evaluation follows the NEMA guidelines. The sensitivity result was 4.79%. They achieved 4.0 mm transverse image resolution and 5.0 mm FWHM axial resolution. The authors claimed they obtained high quality images based on Hoffman brain phantom and 18F-FDG tracer-based patient scans [14].

In another study, Thompson C. J. et al. compared WB-PET and PEM on specific technique for detecting the increased metabolic rate of breast cancer by using a radiopharmaceutical called ^{18}FDG. The comparison proved that PEM is an excellent imaging system for detecting breast cancer than WB-PET Scanner. According to their study, PEM is a low-cost imaging technique and has high spatial resolution compared to the WB-PET scanner. It is 20 times more sensitive than the conventional multi-slice PET whole-body scanner, and it uses less radiotracer which reduces the patient dose and cost per scan [15].

All the above researchers except Musa (Musa et al.) simulated the detector that is placed vertically parallel, at the upper and lower side. By those detectors, only the upper and the lower parts of the breast can be scanned. The detector cannot fully view the side parts of the breast. Therefore, small lesions on the sides of the breast cannot be detected. Musa, et al. simulate cylindrical system PEM scanner but the crystal they used for simulation was expensive. The current research study solves this problem by designing and simulating a high-performance PEM scanner with a cylindrical detector configuration to cover the whole parts of the breast with low cost.

2.1. Photon Detectors

Photon detectors are sensors that respond to electromagnetic radiation for detection and measurement purposes. This is achieved when a high-energetic photon interacts with the surface of a sensing device. Photon detectors measure photon energy and positron and count the incoming photon and photon arriving time. The three main categories of photon detectors are gas-filled, semiconductors and scintillators [16].

2.1.1. Gas-filled Detector

Gas-filled detectors are also called ionization detectors. The gas is located between electrodes having a voltage difference. Those are negative electrodes (cathodes) and positive electrodes (anodes). Gas-filled detectors are further divided into three: Ionization chamber, proportional counter and Geiger Muller (GM) counter. Ionization chambers have been used for many years because of their simple detector mechanism. Figure 1 presents the basic principles of a gas-filled detector.

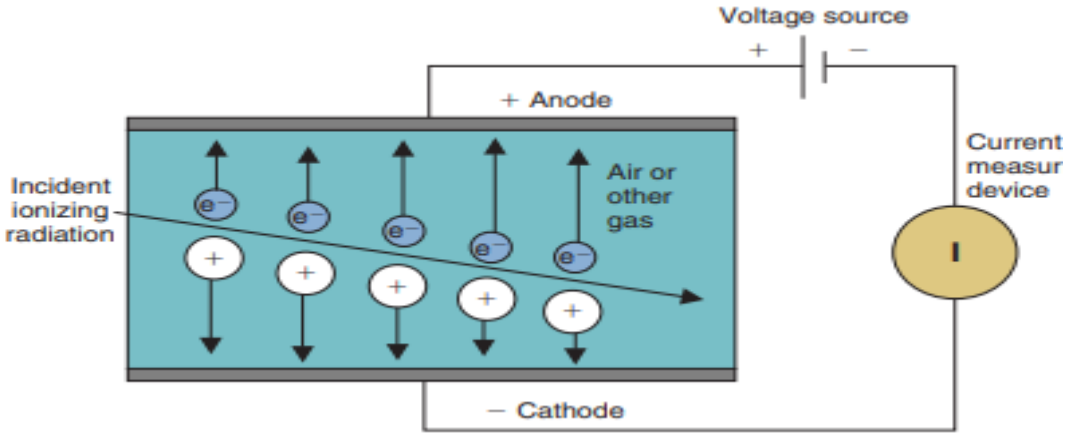

Figure 1: Basic principles of a gas-filled detector (Charry 2012).

Proportional counters have a similar function with that of the ionization chambers. The difference is that they need a more powerful electric field for gas multiplication. The main use of this counter is to distinguish between radiation dose measurement and particle detection [17] and the drawback of this counter is its low efficiency. Geiger-Mulier (GM) counter is designed for maximum gas amplification effect. In the GM and proportional counters, gas amplification occurs. Figure 2 depicts the basic operation principles of the GM counter.

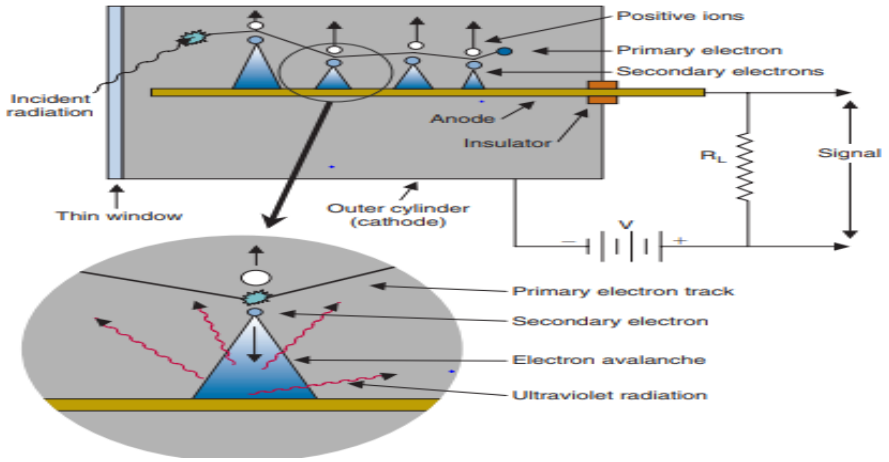

Figure 2: Operating principles of a Geiger-Müller counter (Charry 2012).

The drawback of Gas-filled detectors in nuclear medicine is low detection efficiency and low stopping power.

2.1.2. Semiconductor Detector

Semiconductor detectors have a similar working principle to that of Gas-filled detectors. Semiconductor detectors have similar detection efficiency but better stopping power compared to Gas-filled detectors. That is because semiconductor materials use solid state detector material, denser than gases. This detector works by the ionization process during the interaction between detector material and incident photons. Photon absorption of the detector material caused by the interaction leads to excitation of the valance band electrons. Electrons move to the conduction band and level electron-hole pairs are left at the valance band. As more energy is absorbed by the detector, electron pairs are created and that increases the valance band of the detector [18]. This process is used to prevent recombination [19]. Two types of semiconductors are presented, N-type and P-type. Silicon (Si) and Germanium (Ge) material that are doped with group 5 are N-type while the materials that are doped with group 3 are P-type. A depletion layer (neutral region) is available between the P-type and N-type semiconductors.

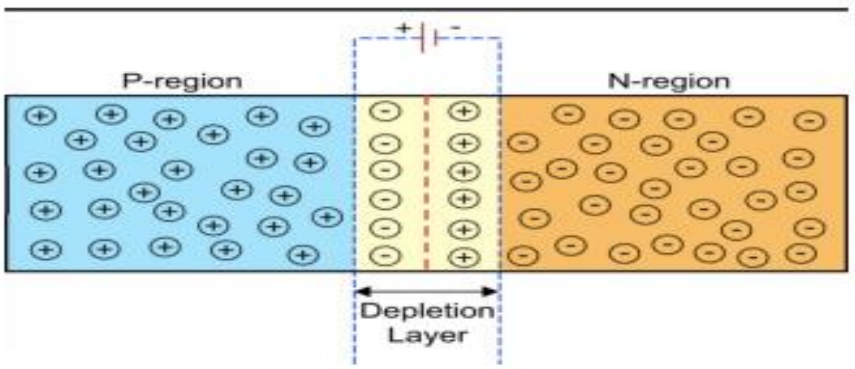

Figure 3: Schematic representation of a P-N junction (Cherry, 2004).

Nowadays, Cadmium telluride (CdTe) and cadmium zinc telluride (CZT) are the most common semiconductor detector materials, besides Silicon (Si) and Germanium (Ge). The major drawback of these detectors is their high cost and low stopping power compared to other scintillator detectors [20]. Table 1 compares properties of four different semiconductor materials.

Table 1: Properties of different semiconductor materials (Takahashi & Watanabe, 2000)

Properties	CdTe	CZT	Si	Ge
Atomic number (Z)	48,52	48,30,52	14	32
Band gap at 300KeV	1.44	1.6	1.12	0.0663
Density (g/cm^3)	5.85	5.81	2.33	5.33
Electron mobility (cm2/Vs)	1100	1000	1400	3900
Hole mobility (cm2/Vs)	100	50	450	1900
Energy resolution (% at 511keV)	1	2-3	0.1-0.3	0.1-0.3

2.1.3. Scintillation Detector

Now a days, scintillation detector materials are the most widely used in radiation detection. They are made of crystals with the attached photo sensor called photomultiplier tube or photodiodes. It works by the luminescence principle. When the incident photons contact the scintillator crystal, energy transfer takes place. Then the crystal absorbs the energy and emit light. This light is detected by the photo-sensor attached to the crystal. The detected light is converted into photoelectrons by the photo-sensors and amplified at varying potential difference within the photo-sensor. Far

ahead, it is collected at the anode part of a photo-detector, where it becomes transformed into an electric signal [21]. Figure 4 presents a typical scintillation configuration with a scintillation material coupled with a photomultiplier tube.

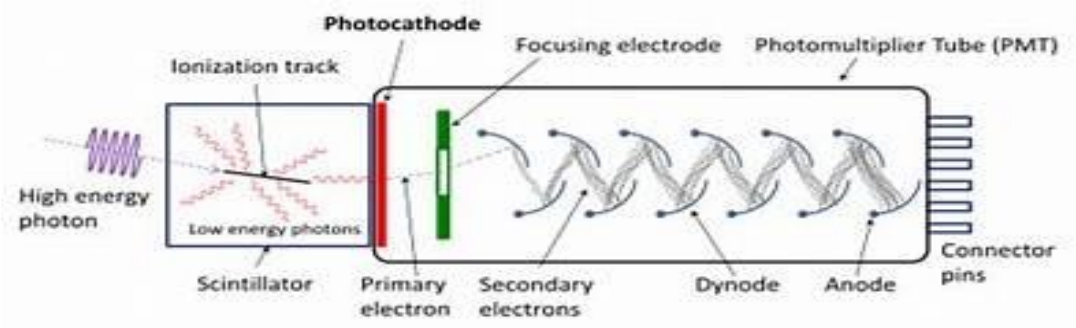

Figure 4: Schematic diagram of a scintillation detector comprising a scintillation material coupled with a photomultiplier tube (scintillator material group 2013).

2.1.3.1. Working Principles of Scintillation Materials

Organic and inorganic scintillators are available. Most of the inorganic scintillator materials are applied in medical imaging. The mode of the scintillators is defined by the crystal lattice, where a definite energy band is allowed to be occupied by electrons [18]. The electron moves from the valance band to the conduction band leaving a gap at the valance band. When electrons return to the valance band, photons are released [18]. The basic working principles of scintillators is shown in Fig. 5.

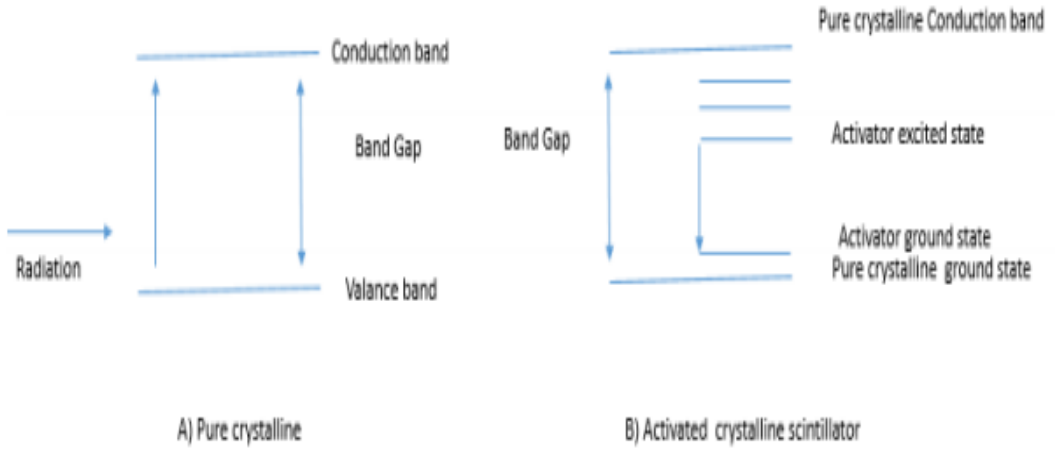

Figure 5: Working principle of scintillators.

2.1.3.2. Characteristics of Scintillator Detector

Categorizing a scintillator material as good or bad is based on the following features: Stopping power, Energy resolutions, Light output, Decay time and Conversion efficiency.

Stopping power: is the capability of the scintillator crystal to diminish the incident photon. It is interrelated to the atomic number and density of the scintillator crystal. If the density of the material is high, it will have a high stopping power. If the material has a high atomic number, it will have a higher detection efficiency. Stopping power is also essential for good image resolution.

Energy resolution: A good energy resolution is better for the proper energy event identification. It is an essential property of a detector material. It helps in measuring the energy of the deposited particle and differentiating the radiations of the varying energies.

Light output: Light output is the number of emitted photons concerning the energy absorbed by the scintillators. A higher light output gives a better spatial resolution. It is linearly related to the energy, the type of incident photon and the conversion efficiency of the scintillator material.

Decay time: It is defined as the time interval between excitation and decay back to the initial state of the atom inside the scintillator material that leads to the emission of light. Short decay time is preferred to have a good coincidence timing. Fast decay time improves fast light production for a better timing resolution.

Conversion efficiency: It is defined by the number of charged particles that are changed to light concerning the absorbed energy of the charged particles. High conversion efficiency is chosen for fast and higher resolution imaging.

Generally, scintillation materials are categorized into organic and inorganic materials. Inorganic materials often need an additional dopant such as cerium (Ce) or Thallium (Tl), which produce the scintillation light. Inorganic groups are characterized by high stopping power, high density, high atomic number and high conversion efficiency for electrons or photons. So, they are the preferred detectors in nuclear imaging applications [21]. Some of the scintillator crystals are NaI (TI) (Thallium doped Sodium Iodide), LSO (Lutetium Oxyorthosilicate), LuAP (Lutetium Aluminum Perovskite), LYSO (Lutetium Yttrium Oxyorthosilicate), BGO (Bismuth Germanate) and GSO

(Gadolinium Oxy-Silicate). Properties of the six mentioned six types of inorganic scintillators are compared in Table 2.

Table 2: Properties of different scintillator crystals (Junwei et al., 2009).

Properties	NaI (TI)	LSO	LuAP	LYSO	BGO	GSO
Atomic number (Z)	71	66	65	60	74	59
Attenuation coeff. (Cm^{-1})	0.34	0.87	0.9	0.86	0.92	0.62
Density (g/cm^{-3})	3.67	7.4	8.34	7.1	7.13	6.7
Index of refraction	1.85	1.82	1.95	1.81	2.15	1.85
Light output	100	75	16	75	15	30
Peak wavelength (nm)	410	420	365	420	480	430
Decay time (ns)	230	40	18	41	300	65
Hygroscopic	Yes	No	No	No	No	No

2.1.3.3. Energy Band Structure of an Inorganic Scintillator

In scintillator crystals, in order to modify the energy structure and the band gap, we need to introduce impurities and the process follows three steps [22]. First, incident radiation energy is absorbed and translated to thermally active electrons and holes. Then the hole and electrons are moved to the luminescence centre, and finally, photons are illuminated. Ionizing radiation creates a charged particle to travel across the crystal material, causing large electron holes. The positive hole ionization fills the activator site. Due to this, electrons are free to move across the material until they find an activation location that is ionized. The electrons travel to the impurity location, forming impurity inside the exciting status. De-excitation happens so rapidly with a possibility of an emitting photon. The use of activating impurity is to change the emitted photons in the visible light range. According to researchers, the typical activator half-life ranges from 7-10s.

2.2. Comparison Between Gas-filled detector, Semiconductor Detectors and Scintillator Crystals

Table 3 below presents comparison between three types of detectors: Gas-filled detector, Semiconductor Detectors and Scintillator Crystals.

Table 3: Comparison Between Gas-filled detector, Semiconductor Detectors and Scintillator Crystals.

Name of the detectors	Description
Scintillator crystals	Have high atomic number, high density leading to high detection efficiency, high light output, are very cheap and they have high capacity of counting rate. Also, they have fast decay time meaning short lifetime of fluorescence, low energy resolution (Avg. 10-14%) and a very good image resolution.
Semiconductor detectors	Have low atomic number, low density (max of 5.85g/cm3) meaning low detection efficiency for 511keV photons, and excellent energy resolution (Avg. 1%) but they are very expensive.
Gas-filled detectors	Have low detection efficiency and low stopping power.

2.3. Optical Transparent Ceramic (TOC) Scintillators

Optical transparent ceramic scintillators (TOC) are recently introduced cerium doped alkaline earth hafnate scintillators. They are used in high-energy physics applications. These new scintillators are used for PET and SPECT imaging because of their high stopping power (high density and high atomic number), good light output and for being non-hygroscopic [23]. They also have fast decay time for high-performance PET imaging system design [24]. TOCs are presented with the composition of materials containing cerium and hafnate with alkaline earth metals. The TOCs considered in the current study are cerium doped lutetium hafnate – LHO ($Lu_2Hf_2O_7$: Ce), cerium doped strontium hafnate – SHO ($SrHfo_3$: Ce) and cerium doped barium hafnate – BHO ($BaHfO_3$: Ce).

Edgar Van Loaf et al. studied properties of cerium doped strontium hafnate SHO and cerium doped barium hafnate BHO of TOCs including their Pulse hight, scintillation

decay and time spectra compared them with BGO. They found out that TOCs have good transparency compared to BGO and it is significant for PET imaging. The light yield of BHO and SHO is approximately 40,000 photons/MeV compared to BGO which is 2-3 Photon/MeV [23]. LHO is the same as BGO in terms of light yield. The decay times of BHO and SHO are 25 ns and 42 ns, respectively [24].

Woody et al. studied the morphology, transparency and optical properties of SHO compared to BGO. They proved that SHO has good transparency and resealable light yield several times BGO. They claimed that if ceramic is produced with large quantities and size, they will have to be considerable interest for PET as well as CT [25].

The research team who had a patent from USPAP described that TOCs have relatively high output and short decay time compared to other scintillators. And also has an excellent scintillator property compared to BGO. They proved it used for medical imaging applications. Table 3 presents ceramic doped alkaline earth scintillators' properties.

Table 4: Property of ceramic doped alkaline earth scintillators.

Property	NaI NaI: TI	BGO $Bi_4(GeO_4)_3$	GSO: Ce Gd_2SiO_5: Ce3+	LSO: Ce Lu_2SiO_5:Ce3+	TOCs
Density (g/cm3)	3.7	7.1	6.7	7.4	7.7- 8.4
Attenuation coefficient at 511 Kev(cm-1)	0.37	0.95	0.70	0.89	0.85-0.95
Relative light output (%)	100	7 – 12	30	30	20 – 30
Light yield (10^3photon/MeV)	38	2-3	8-10	30	40
Decay time (ns)	230	300	40	40	10 – 45

In this thesis work, the PEM design and simulation uses these TOCs scintillator materials because of their high density and short decay time.

2.4. Nano-material Based Scintillator

Now-a-days there are novel Nano material scintillators, such as Terbium-doped $LiYbF_4$ nanomaterial, which are high quality scintillator crystals. They are used for medical applications, safety inspection and industrial applications [26].

2.5. System Design and Breast Size Calculation

Calculation of the radius of the cylinder was based on the average breast size. Deirdre E. et al., 2010, researched on the breast volume to find the correct fitted bra size for women. Their measurement samples were taken from 104 women with different breast sizes with a mechanism of water displacement, has also been shown in Fig. 6 [27].

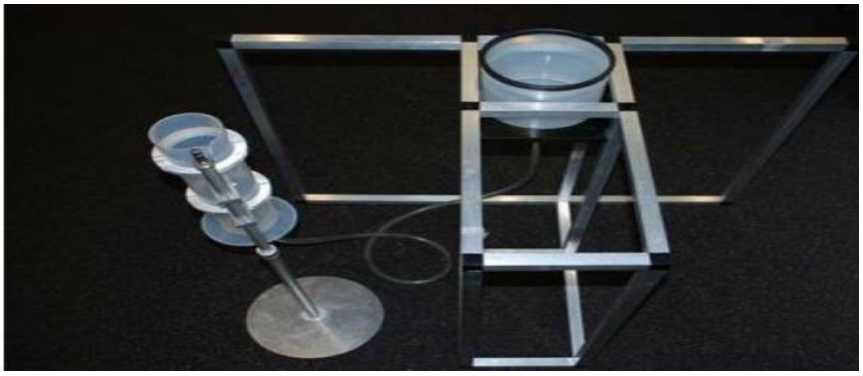

Figure 6: The custom-designed water displacement device used to measure breast volume.

According to their finding, the mean breast volume of left breast was 642 ml, and the right breast was 643 ml with ranges between 25 ml (10A bra size) to1900 ml (24DD bra size) of Australian sizing. The cup size is computed using the following formula:

$$Cup\ Size = Bust\ Measurment - Band\ Mesurement \qquad \text{Equation 1 [28]}$$

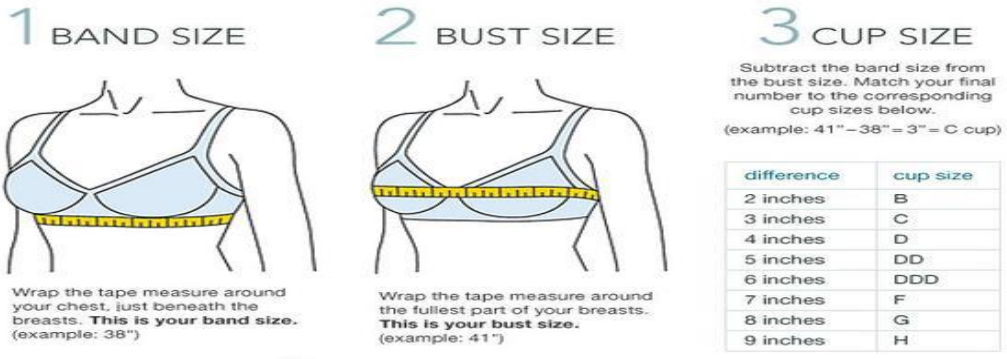

Figure 7: Breast size measurement for bra cup calculation (Dor-Ne Corset shoppe, established in 1932).

In order to design the proposed PEM scanner in the current work, the mean value of the breast volume statistical data was considered. The breast is assumed to be an irregular cylinder and the mean volume of the left and right breast are calculated as:

$$Avarage\ of\ breast\ volume = \frac{left\ breast\ size + right\ breast\ size}{2} \quad \text{Equation 2}$$

Volume of cylinder = π *square of the radius *height of the cylinder

$$V = \pi r^2 h \quad \text{Equation 3 [29]}$$

where π=3.14, r= radius and h= height of the cylinder

Assume radius of the breast is approximately equal to its height, the volume becomes:

$$V = \pi r^3 \quad \text{Equation 4}$$

2.6. National Electrical Manufacturer's Association (NEMA) Standard

There is a standard for performance testing of PET and SPECT scanners that have been developed by National Electrical Manufacturer's Association (NEMA). The available standards include for both small animal PET and whole-body PET systems. NEMA has different versions. In the current thesis work, the NEMA NU4-2008 standard has been followed that is often used for small animal PET [30]. In order to do system performance evaluation, the size of small animals was approximated to breast size. By using this standard, different performance matrices including sensitivity, scattering fraction, spatial resolution, image quality and uniformity were computed.

2.6.1. Sensitivity

Sensitivity is expressed as the rate in counts per second and its unit is counts per second per Becquerel (cps/Bq). It is the ability of a scanner to detect true coincidence photons from inside the FOV of the scanner. The geometry of the scanner and stopping power of the detectors can mainly affect the sensitivity of the system. The small diameter geometry and the large FOV have higher sensitivity. When the sensitivity is high, the signal to noise ratio in the reconstructed image is also high. The sensitivity (*Si*) at each pixel position *i* is given by:

$$Si = \frac{R_i - R_{B,i}}{Acal} \quad \text{Equation 5 [31]}$$

where R_i is the total count rate (cps) that is collected with source position (slice), $R_{B,i}$ is the background event rate collected without source in the scanner FOV, and $Acal$ is the source activity in Becquerel (Bq).

For acquisition *i*, the absolute sensitivity (in percentage) is given by:

$$S_{A,i} = \frac{S_i}{0.9060} x100 \qquad \text{Equation 6 [31]}$$

where 0.9060 is the branching ratio of ^{22}Na. The total sensitivity is determined as:

$$S_{tot} = \frac{1}{N}\sum_i Si \qquad \text{Equation 7 [31]}$$

$$S_{A,tot} = \frac{1}{N}\sum_i S_{A,i} \qquad \text{Equation 8 [31]}$$

where N is the total number of image slices.

The sensitivity test requires a ^{22}Na point source of less than 0.33 mm diameter with the activity of 24.5KBq inside the 10 x 10 x 10 mm acrylic cube. For the first measurement, the source is positioned at the Central FOV of the system.

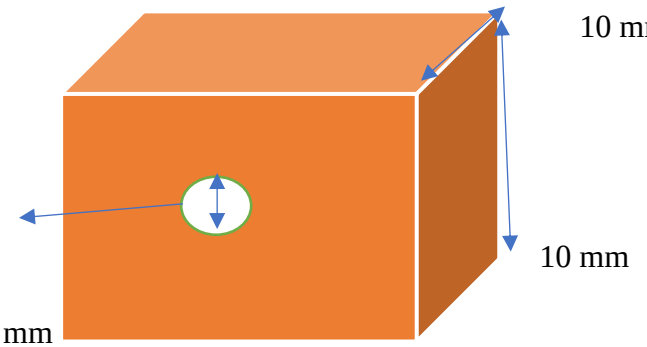

Figure 8: Sensitivity measurement phantom acrylic cube.

2.6.2. Scattering Fraction

A scattering fraction test is made to recognise the designed PEM system sensitivity for the scattered photon. This characterization of the system is done at minimized counting rate aiming at reducing the effect of random events, dead-time, and collision. A lower scattering fraction is preferable. The scattering fraction (SF) is determined as:

$$SF = \frac{\sum i \sum_j C_{r+s,i,j}}{\sum i \sum_j C_{tot,i,j}} \qquad \text{Equation 8 [31]}$$

where C_{r+s} is the scatter counting for slice i^{th} in j^{th} acquisition, and C_{tot} is the total counting from the true count and the scattered. In the current thesis work, in order to calculate the scattering fraction of the PEM scanner by NEMA NU4 2008 standard, a cylindrical phantom has been used. It is made of polyethylene with a dimension of 70 ±0.5 mm in length and 25±0.5 mm in diameter. There is another cylinder inside the big cylinder which is 3.2 mm in diameter opening at a 10 mm radial location, and it is aligned parallel to the central axis with 60 mm long axial width. The source type used in the system was 18F. A schematic of the SF measurement cylindrical phantom is shown in Fig. 9.

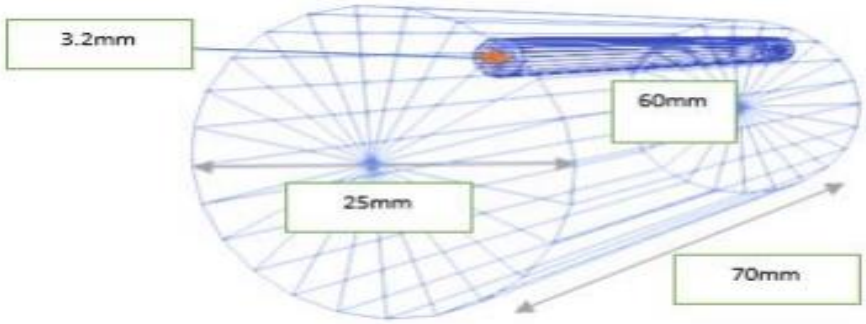

Figure 9: SF measurement phantom.

2.6.3. Spatial Resolution

Spatial resolution is the ability to distinguish two points in the image. Spatial resolution is measured by using image point source in a scattered medium and reconstructing the image without image smoothing process. The purpose of measuring the spatial resolution is to characterize the width of the point spread function (PSF) of the radioactive source. The width of the PSF is defined by its full-width at tenth-maximum amplitude (FWTM) and full-width at half-maximum amplitude (FWHM). In the current thesis work, a 3D direct Fourier based image reconstruction algorithm was used with 1.0 mm slice thickness.

2.6.4. NEMA Image Quality

The test is performed using a phantom made of poly-methyl-methacrylate having three compartments as shown in Fig. 10: a uniform region source filled with ^{18}F, fillable five rods of size 1mm to 5mm, and the third compartment made of two chambers, one filled with air and the other with water while the chambers are immersed inside a uniform

region filled with ^{18}F. The phantom has a cold top. The rods and the uniform parts of the phantom are filled with ^{18}F radionuclide with the activity source of 3.7 MBq. According to NEMA NU4 2008 standard, 10 million events are needed for image reconstruction. In the current thesis work, a 3D direct Fourier reconstruction algorithm, with 1.0 mm slice thickness was used without correction to reconstruct the image.

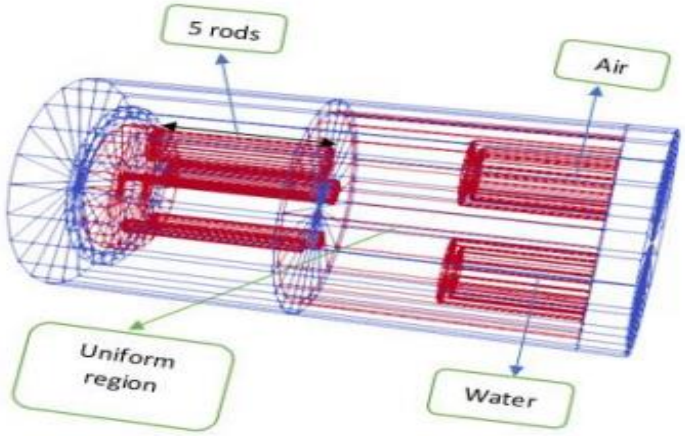

Figure 10: NEMA image quality phantom.

2.5.5. Uniformity

The uniformity test measures how uniform the sensitivity of the system is. It is evaluated by moving the source every 10 mm away from the centre.

CHAPTER THREE

OVERVIEW OF PET IMAGING TECHNIQUES AND PEM IN NUCLEAR MEDICINE AND IMAGE RECONSTRUCTION MECHANISMS

3.1. History of Nuclear Medicine Imaging

The origin of nuclear medicine was introduced in the nineteen centuries. In 1896, Henri Becquerel discovered radioactivity. In 1898, Marie Curie discovered Radium. These developments provided an idea of the discovery of X-rays by Wilhelm Roentgen in 1895. Both X-rays and radium sources were rapidly adopted for medical applications. In nuclear medicine, the two-wide class of imaging are single-photon imaging and positron imaging [32]. Single-photon imaging of single-photon emission computed tomography (SPECT) uses radionuclides that decay by gamma-ray emission. For SPECT, data are collected from many different angles around the patient body. That allows cross-sectional images of the radionuclide distribution to be reconstructed, thus providing the depth information missing from planar imaging. Positron imaging of positron imaging tomography (PET) uses radionuclides that decay by positron emission. The emitted positron consumes a very short lifetime and annihilates with an electron. At the same time, it produces two high-energy photons that subsequently are detected by an imaging camera. Tomographic images are formed by collecting data from many angles around the patient, resulting in PET images. In late 1920, Positron was introduced for the first time. In 1932, Deric experimentally checked it by using the idea of quantum mechanics and special relativity combination. In 1913, Georg de Hevesy developed the tracers' biological approach and principle. After studying the absorption and translocation of radioactive lead nitrate in a plant, the tracer starts to be applied in the biological system by 1923 [33]. In 1927, Blumgart and Weiss studied the radioactive tracers for the first human. In the 1930s, Lawrence invented the cyclotron [34] (please see Fig. 11).

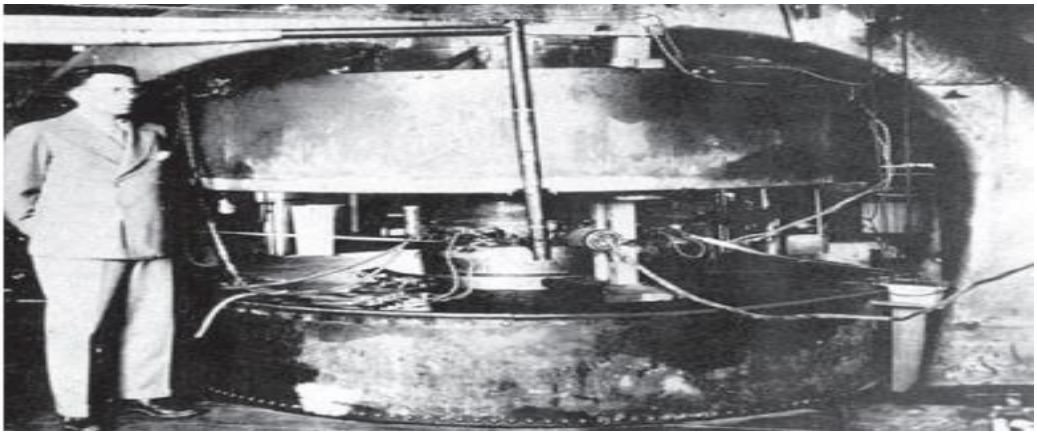

Figure 11: Ernest O. Lawrence standing next to the cyclotron he invented at Berkeley, California (Lawrence EO, 1932).

In the 1950s, the technology was developed and they obtained image of the distribution of radionuclides in the human body rather than counting at a few measurement points. In 1951, Benedict Cassen developed most important millstones that included rectilinear scanner.

Figure 12: Benedict Cassen with his rectilinear scanner (1951) (left) and thyroid scans from an early rectilinear scanner (Cassen B, 1951) (right).

In 1951, Wrenn and his co-workers described the use of positron emitters and their advantages in imaging properties of those radionuclides [32]. In 1952, the first clinical PET device was built (see Fig. 13). It was based on the same concept as that produced in 1950, but it included some changes. Low resolution images were obtained with such device, and the sensitivity suggested the existence of a tumour.

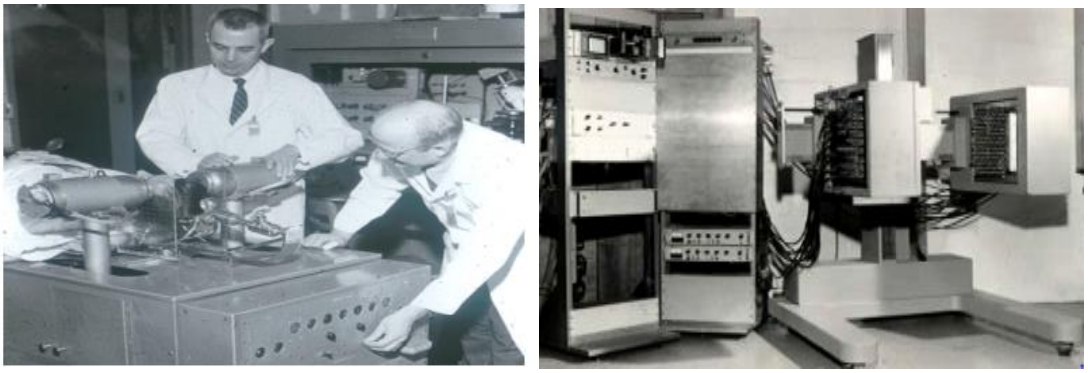

Figure 13 : First clinical PET ("First clinical positron imaging device", 2017).

In 1958, Hal Anger with the first gamma camera as presented in Fig 18. In 1971, Vanderbilt University Hospital scan brain by using ^{99m}Tc (see Fig 14).Until 1960s, ^{131}I had a great role in the nuclear medicine field. It was used primarily for the diagnosis and study of thyroid disorders. In 1964, Paul Harper and colleagues changed to the use of the gamma ray emitted ^{99m}Tc for imaging in nuclear medicine. It proved to be very flexible for the classification of a wide variety of compounds that could be used to train virtually every organ in the body. It had a good property for imaging. Nowadays, it is the most widely used radionuclides in nuclear medicine [35].

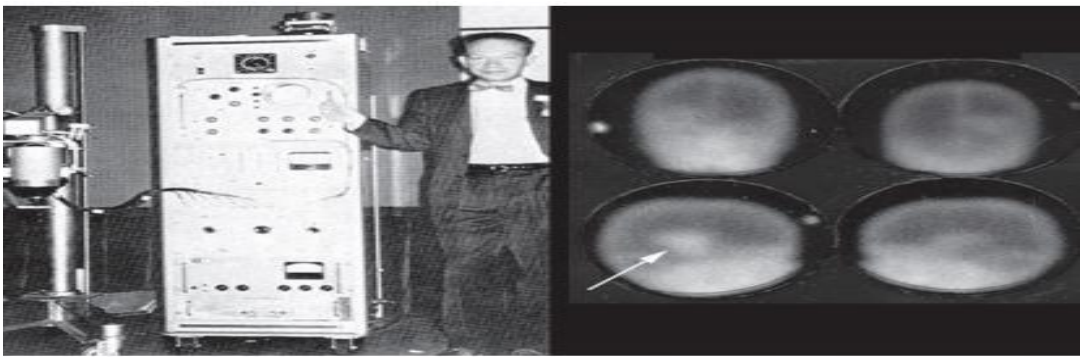

Figure 14: Hal Anger with the first gamma camera in 1958 (left) and 99mTc-pertechnetate brain scan of a patient with glioma at Vanderbilt University Hospital (1971) (right).

Currently, Nuclear medicine is used for a wide variety of diagnostic tests. In 2006, 100 different diagnostics procedures took place with radionuclides. In 2008 more than 30 million procedures were performed, 20,000 nuclear medicine camera and 3000 PET scanners were installed in the hospitals worldwide. Over 4 million PET procedures were performed annually [10].

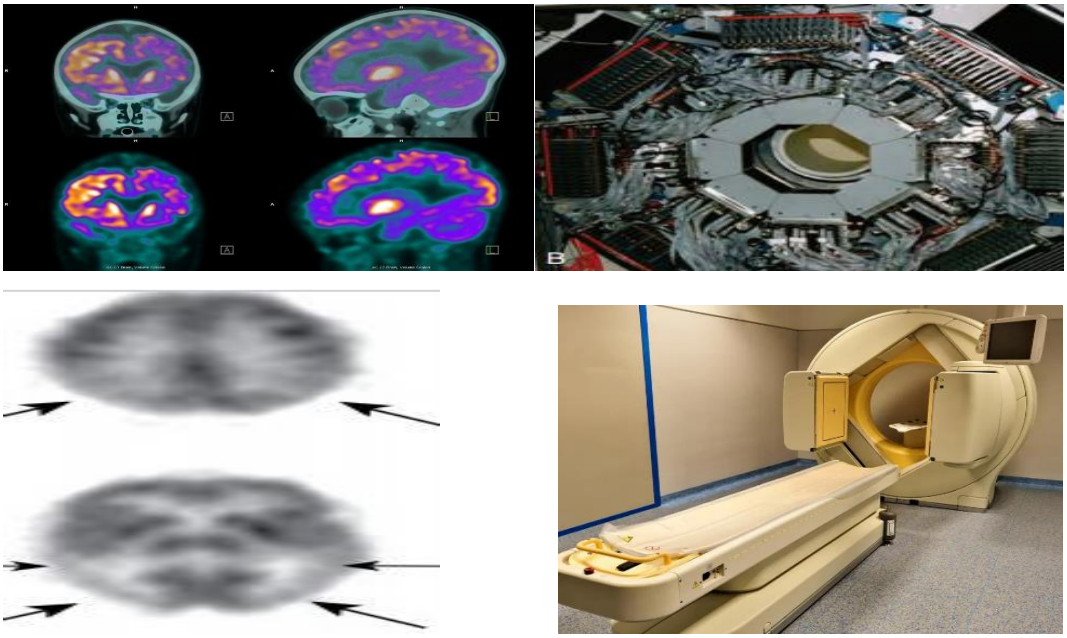

A B

Figure 15: A, brain image and Alzheimer disease at earlier stage (http://mayoclinic.org/test-procedure), B PET scanner interior and exterior image PET scanner with detectors

3.1.1. Conventional Nuclear Medicine Imaging with SPECT

Single photon emission computed tomography (SPECT) is a non-invasive nuclear medicine imaging device for visualizing deferent organ functions. Most common radioactive isotopes used in SPECT is ^{99}Tc.

3.1.2. Molecular Imaging with PET

PET is one molecular imaging technique in nuclear medicine imaging. Recently, a specific probe has been developed for positron emitting radionuclides. PET is used to diagnose different organs such as breast, brain and the heart.

3.2. Working Principles of PET and Annihilation Coincidence Detection

3.2.1. General Working Principles of PET

Imaging procedures in nuclear medicine are non-invasive and painless. PET is one of the nuclear imaging techniques that uses a radioactive tracer to provide an image of

living organs and tissues. Depending on the body part to be examined, the radiotracers are swallowed, inhaled, or injected into the vein. Currently, ^{18}F-fluoro-2-deoxy D-glucose (FDG) is commonly used radiotracer. It is injected to the blood-stream via vain. Due to their higher affinity to absorb glucose, tumour cells absorb more radiotracers than normal cells. When radiotracer is injected to the blood stream, beta decay will occur and emit a positron (e^+) [10].

As a nuclear transformation emits a positron, the positron scatters through matter, losing its energy. It annihilates with an electron, resulting in two 511-keV photons emitted in nearly opposite directions, has also been shown in Fig. 14.

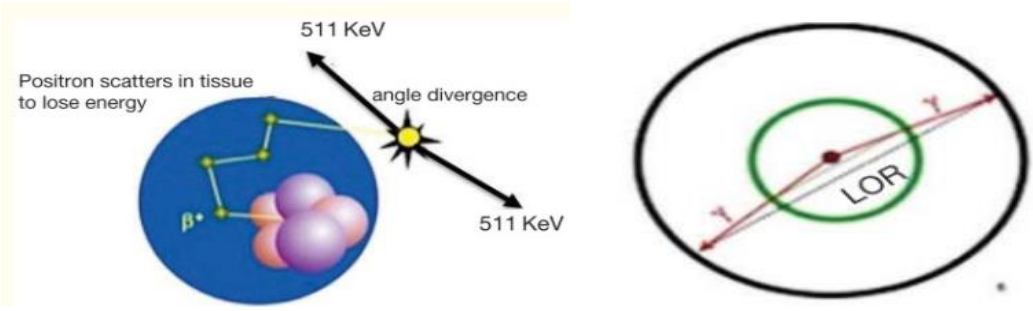

(b)

Figure 16: (a) Annihilation coincidence detection (ACD), (b) Line of response (LOR). (Galal Omami et al. 2014).

A PET scanner is usually used to measure the amount of consumption of glucose. It consists of numerous rings of detectors that rotate around the patient. The detector may be made up of scintillator crystals or semiconductor detectors. That electronically coupled opposing detectors simultaneously identify the pair of gamma ray by using coincidence detection circuit which measures annihilation events within 10 to 20 ns. The general working principles of PET is depicted in Fig.15.

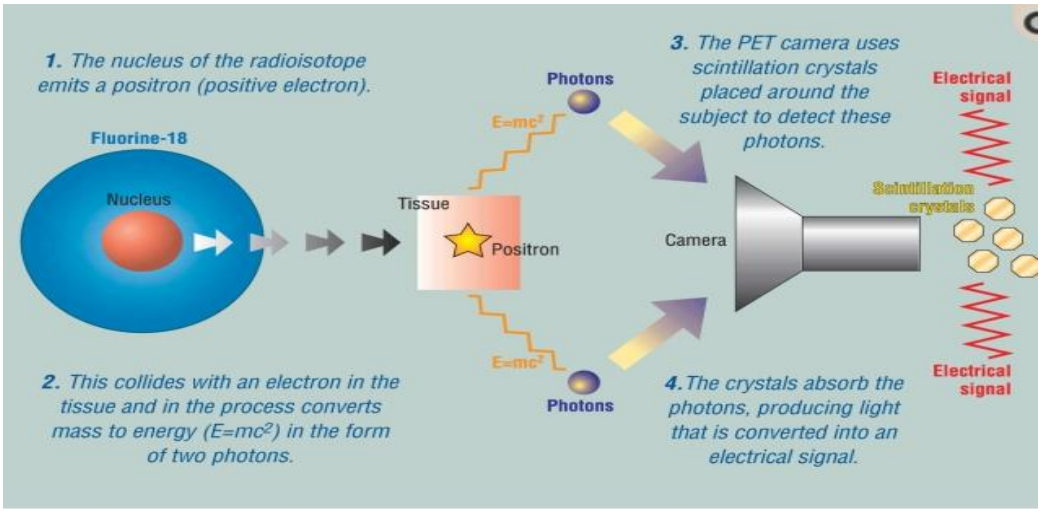

Figure 17: Working principles of PET (BMJ, 2003).

The PET scan data consists of several coincidence lines, recognized as projections. Those data are processed by using iterative reconstruction or back-projection algorithm to form the number of connecting axial slices [36]. Figure 16 presents a typical brain image constructed using a PET scanner.

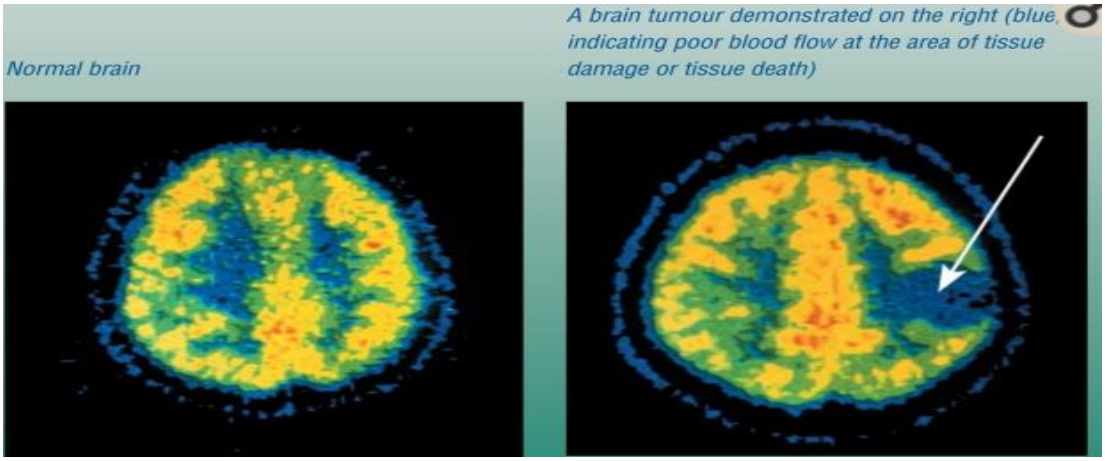

Figure 18: PET scanner brain image (National Cancer Institute/SPL).

3.2.2. Events type in Annihilation Coincidence Detection

There are different types of coincidence events that occur during PET scanning. Those are true coincidence, scattered coincidence and random coincidence events (see also Fig. 10).

True coincidence: is also called prompt coincidence. It occurs when both photons from an annihilation event are detected.

Scattered coincidence: is also called invalid prompt coincidence. It occurs when one or both photons from annihilation events outside the volume for true coincidence events commence/s scattering.

Random coincidence: is also called accidental coincidence. It occurs when two different positron annihilation events occur. Annihilation photons are detected in two different detectors with in the coincidence window recorded as a single coincidence event [10]. Figure 17 presents types of coincidence event in PET scanner.

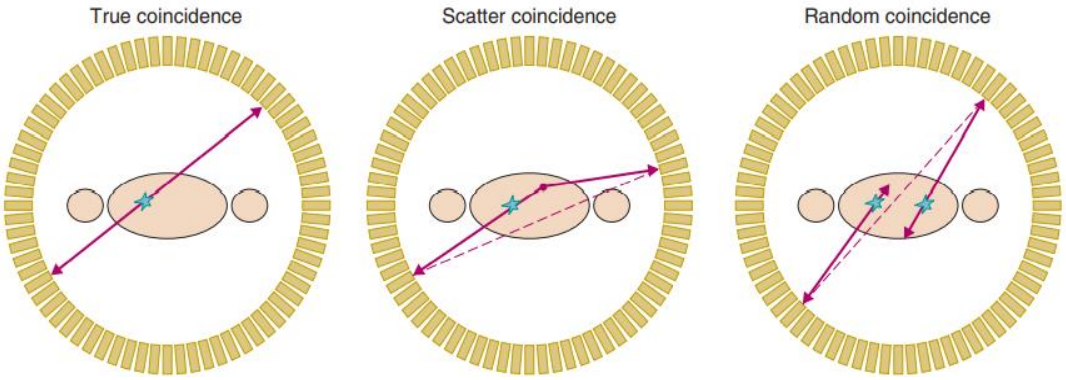

Figure 19: Detected events in PET explaining the three types of coincidences (Chery 2012).

The valid events (coincidences) fulfil the following conditions [6]:

Condition 1: The formed LOR (dotted lines in Fig. 10) by both photons is inside a valid acceptance angle of the system.

Condition 2: The photon energy kept on the crystal drops inside the chosen energy window.

Condition 3: Two photons are detected within a recognized coincidence time window.

3.3. Radiopharmaceuticals in PET/SPECT Scanner and Cyclotron

Radiopharmaceuticals are chemical substances used for PET imaging. When tagged as a radionuclide, they are used for diagnosis and treatment purposes. There are different radionuclides available in the market that are used to diagnose and treat different organs. Radioactive iodine (I-131) is a type of radiotracer often used to treat cancer on the thyroid gland and other organs. The patient who cannot respond to chemotherapy (for example, non-Hodgkin's lymphoma patients) could undertake radio immunotherapy

(RIT), which is a personalized cancer treatment. It combines radiotherapy with the targeting ability of immune system. F-18 fluorodeoxyglucose (^{18}FDG) is the common radiotracer used to diagnose cancers of the tissues. Currently, 95% of radiopharmaceuticals are used for diagnosis and around 5% for therapy purposes [37]. Cancer cells absorb more glucose than that of normal cells because of their high metabolic activity [35]. Table 4 lists different radioisotopes available in the literature including their lifetime as well as common uses.

Cyclotron is a machine that is used to accelerator ions/charged particles to high energies called radionuclide. To increase the energy of the particles, it uses magnetic and electric field.

Table 5: Radioisotopes and their use in nuclear medicine (Cyclotron Produced Radionuclide IAEA VIENNA, 2008)

N_o	**Radioisotope**	**Lifetime**	**Uses**
1.	Cobalt-57	272 days	✓ as a marker to estimate organ size ✓ as invitro diagnostic kits
2.	Iodine-123	13 hours	✓ for diagnosis of thyroid function ✓ it is a gamma emitter without the beta radiation of I-131
3.	Gallium-67	78 hours	✓ for tumour imaging ✓ for localization of inflammatory lesions (infections)
4.	Technetium-99m	6 hours, derived from Mo-99 parent (66 h)	✓ to image the skeleton and heart muscles ✓ sometimes it is used for brain, thyroid, lungs (perfusion and ventilation), liver, spleen, kidneys (structure and filtration rate), gall bladder, bone marrow, salivary glands, heart blood pool and infections ✓ for numerous specialized medical studies
5.	Indium-111	67 hours	✓ for specialized diagnostic studies, e.g., for the brain, infections and colon transit
6.	Carbon-11 Nitrogen-13	20.4 min 9.97 min	✓ for positron emitters used in PET for studying brain physiology and pathology,

	Oxygen-15 Fluorine-18	2 min 110 min	in particular for localizing epileptic focus, and in dementia, psychiatry and neuropharmacology studies ✓ Fluorine-18 in FDG in detecting cancers and in monitoring progress in their treatment, in PET
7.	Krypton-81m	13 sec from Rb-81 (4.6 h hours)	✓ For functional imaging of pulmonary ventilation, e.g., in asthmatic patients, and for the early diagnosis of lung diseases and function
8.	Strontium-92	25 days	✓ As the 'parent' in a generator to produce Rb-82.
9.	Rubidium-82	65 hours	✓ Is convenient PET agent for myocardial perfusion imaging
10.	Thallium-201	73 hours	✓ For diagnosis of coronary artery disease and other heart conditions, such as heart muscle death and for location of low-grade lymphomas.

From the listed radiotracers in the above table, Tc-99m, I-123, Tl-201, and Ga-67 are the most commonly used for SPECT. C-11, F-18, Rb-82, and N-13 are used for PET imaging. Radionuclides are also used for industrial applications. Such as material processing, quality control, environmental/biological applications, agricultural applications, insect control and plant physiology study [37].

3.4. Applications of PET scanner

3.4.1. Clinical Applications of PET

PET scanner is used to diagnose Alzheimer's disease, brain Neurological conditions (such as Parkinson's disease), Huntington's disease (hereditary disease), Epilepsy (a brain disorder involving recurrent seizures), Cerebrovascular accidents (stroke), and is also used to diagnose tumours of different human organs. Other clinical applications of PET include: evaluate the effectiveness of cancer treatment, follow-up the progress of

cancer lesions after treatment and detect return of tumours better than other diagnostic modalities, show and locate the specific surgical site prior to surgical procedures of the brain, evaluate the brain after trauma to detect hematoma (blood clot) and/or bleeding, detect and evaluate blood and oxygen flow inside the brain tissue, detect the spread of cancer to other parts of the body from the original cancer site, evaluate the perfusion (blood flow) to the heart muscle (myocardium), detect prostatic cancer, breast cancer and uterus cancer, further identify lung lesions or masses detected by X-ray and/or CT and assist in the management and treatment of lung cancer by staging lesions.

3.4.2. PET in Research

PET technology has been applied in pre-clinical use and small animal PET in the laboratory. It is applied in creative ways to study drug actions in the human body through obtaining knowledge on the movement of drugs/pharmacokinetics and their therapeutic, toxicity and adverse effects. It has also been used to study the physiology and genes of small animals and the development of new radiotracers [38].

3.4.3. Hybrid PET Imaging

Currently, developmental movement in PET is the hybrid imaging technology that includes PET/MRI, PET/CT and time-of-fight (TOF) PET systems. The hybrid system is a new technology in nuclear medicine. It combines radiation devices with nuclear medicine devices by using spatial software. For example, PET/CT hybrid imaging technique is a combination of CT and PET. In the late 1990s, David Townesend and his colleagues developed the prototype for hybrid PET/CT [10] [39]. In this mechanism, anatomical images from CT scan are combined with the metabolic images obtained from PET. The patient takes the radiotracer, and after a while, the patient is placed on to PET/CT bed. Then the scanning starts from the CT component to acquire X-Ray and afterward PET component scan to acquire a metabolic image. The hybrid approach is very important to determine a better localization and metabolic activity. Figure 18 presents a typical PET/CT imaging device.

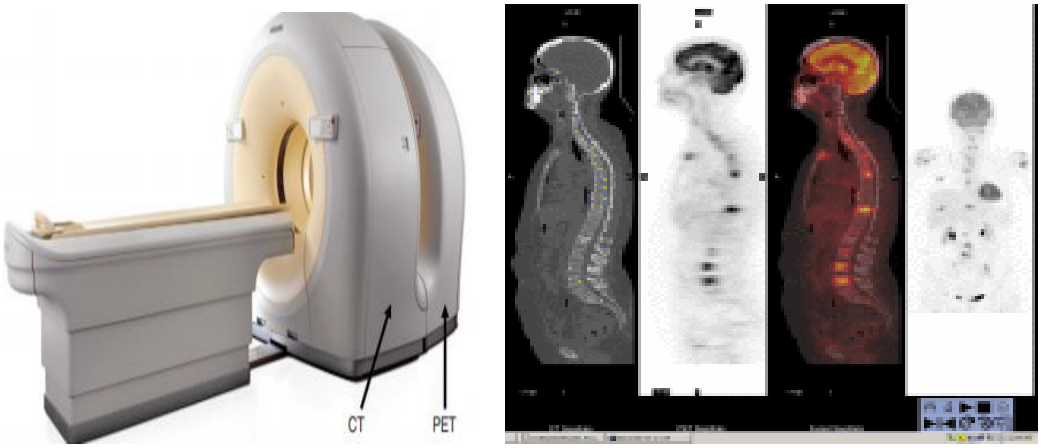

Figure 20: (left) Hybrid PET/CT scanner. The axial separation between the PET and CT components is adjustable (Courtesy Philips online.), and (right) detection of bone metastases in breast cancer patients using the PET/CT (M. Caglar et al., October 2015).

PET/MRI is another hybrid technology that is very important for an easy view of scanned anatomical and metabolic activity of both small animals and the human body. In 2005, the first practical hybrid PET/MRI was developed (see Fig.21). [40] [39].

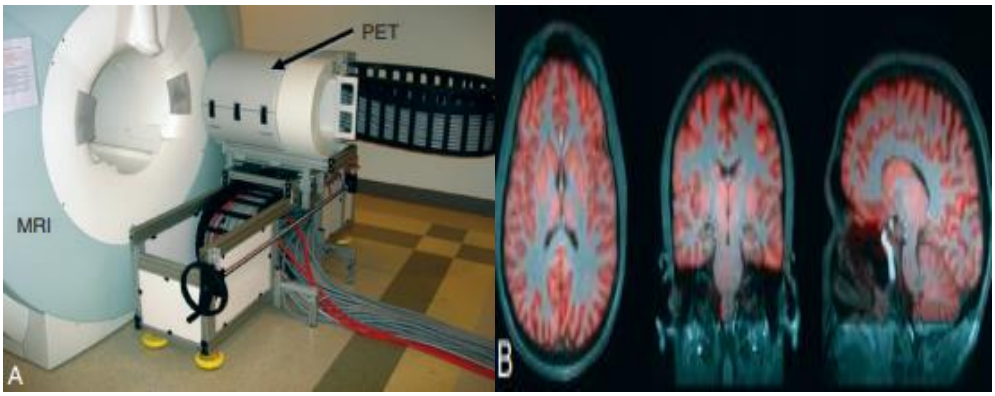

Figure 21: (A) Hybrid PET/MRI scanner. The PET scanner is inserted inside the bore of the magnet to allow simultaneous acquisition of PET and MRI images of the brain. The field strength of the MRI scanner is 3 T, (B) simultaneously acquired 18F-fluorodeoxyglucose.

3.5. Positron Emission Mammography

3.5.1. Mammography

Mammograph is a non-invasive device of low dose X-ray up to 30kVP to diagnose and screen breast cancer. Mammography is specialized medical imaging technique used to visualize the breast and diagnose breast cancer.

3.5.2. Positron Emission Mammography

Positron emission mammography (PEM) is an imaging device that works on positron emission by annihilation process to image breast cancer. First, the patient takes an injection of radionuclide called radiotracer. After a while, the patient's breast is scanned by a PEM scanner. The cancer area absorbs more glucose, and it is seen as the bright spot in the PEM image. In this process, positrons are emitted in the positive beta decay of radioactive nuclei. Figure 22 presents a PET scanner used for imaging of the breast.

Figure 22: A PET system designed for breast imaging. Two detector panels scan back and forth to acquire an image of the breast under mild compression. (Courtesy Naviscan Inc., San Diego, CA).

Wendie A. Berg et al., did comparison between PET and PEM. They scanned 94 women with cancer by using high resolution PET scanner and fluorodeoxyglucose (FDG) with PEM scanner. The study proved that FDG PEM has high diagnostic accuracy for breast lesions [41].

3.6. Image Reconstruction Techniques in Tomography

3.6.1. Definition of Projection, Line of Response, and Sinogram

Projection: Is a group of lines of response that are recorded at some angle at the detector.

Line of Response (LOR): is the line that connects the two detectors during the coincidence annihilation photons. Based on LOR, we might get information about where coincidence events (annihilations) take place.

Sinogram: is a sinusoid curve derived from row data histogram. The sinogram is produced by a point source object located in specific position as also been shown in Fig. 23. It is the matrix of the projection from several angles [42].

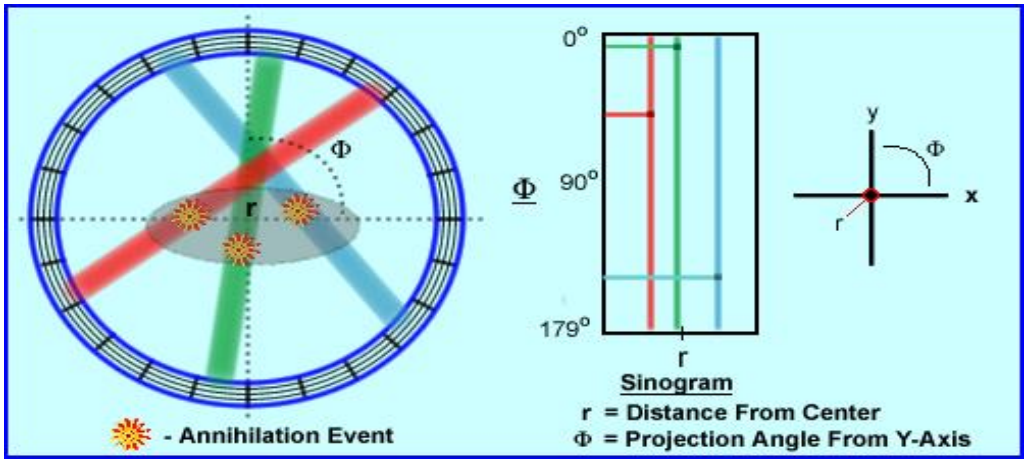

Figure 23: Sinogram formation and annihilation event.

3.6.2. Filtered Back Projection

The goal of reconstruction in tomography is to generate a 2D cross-sectional image of activity from the slice of the object, f(x,y), using a set of projection profiles (sinogram) that are obtained from the slice. That all projection profiles build up the back-projected image as also depicted in Fig. 24.

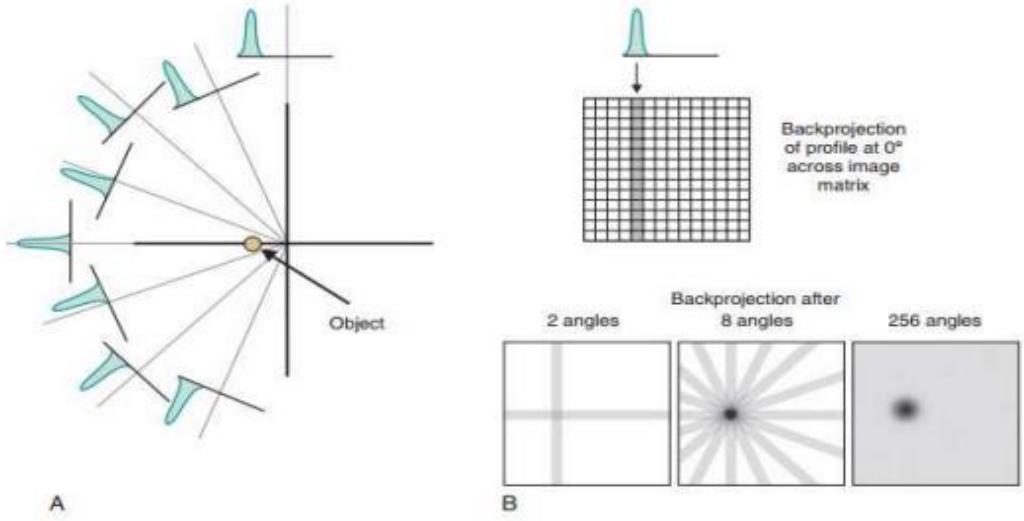

Figure 24: (A) projection profiles for a point source of radioactivity for different projection angles, and (B) Back projection of one intensity profile across the image (Charry, 2004).

3.6.3. Direct Fourier Transform (FT) Reconstruction

The method involves calculation of the 1D FT of the projection followed by the 2D inverse FT [10]. The projection theorem, Central or Fourier Slice Theorem (CST) facilitates the process. First, the one-dimensional Fourier transform of the projection data is calculated in a polar grid. Each projection is placed in its corresponding angle. This is followed by resampling in a Cartesian grid using interpolation (linear, nearest neighbour, splines, etc). Finally, the two-dimensional inverse Fourier transform is utilized to obtain the reconstructed image.

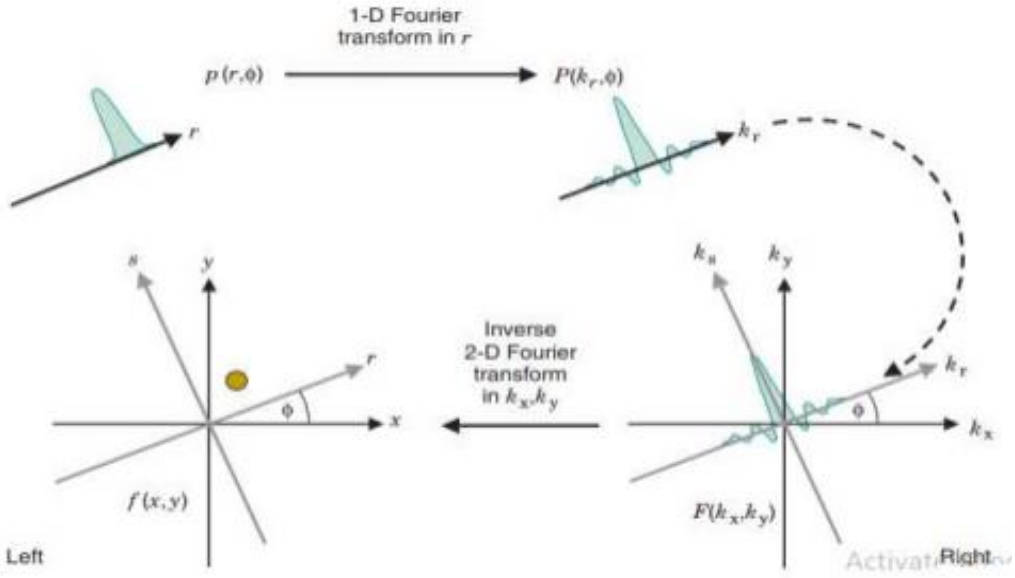

Figure 25: Implementation of the direct Fourier transform reconstruction (Charry 2004).

3.6.4. Iterative Image Reconstruction

Compared to the other reconstruction techniques, iterative image reconstruction (IIR) is believed to be more flexible. The process is depicted in Fig. 26 below. As opposed to the analytical reconstruction methods like back projection, iterative reconstruction techniques optimize an objective function iteratively. This objective function consists of data fidelity and an edge-preserving regularization term. The optimization process involves forward and backward iterations between image space and projection space [10].

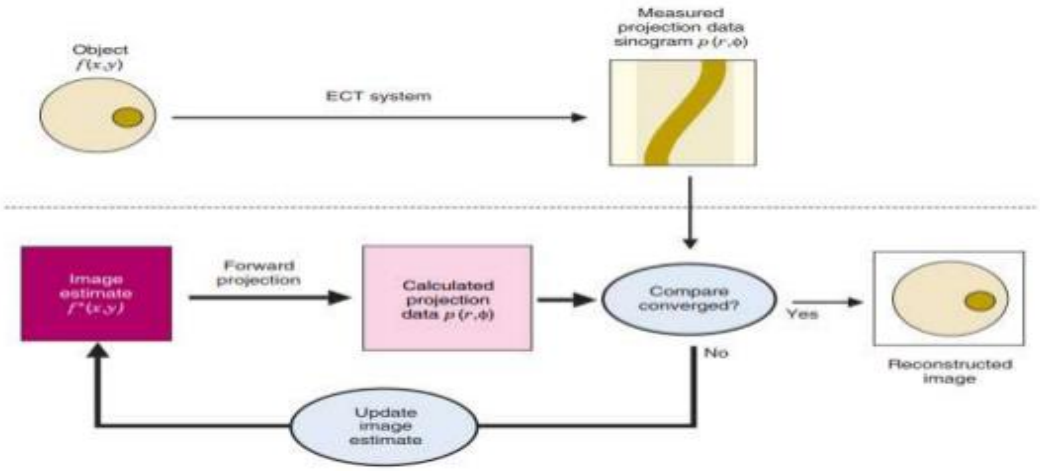

Figure 26: Steps in iterative image reconstruction (IIR) (Cherry 2012).

3.6.5. Maximum Likelihood Expectation Maximization (ML-EM)

In this method, the recorded projection data is reconstructed based on an iterative approach. The statistical approach based on the maximum likelihood principle is implemented to distribute and approximate the source. In this process, the impact of counting state is taken into account. That involves tagging a reduced weight to low count and a greater weight to high count [16].

3.6.6. Ordered Subset Expectation Maximization (OS-EM)

In this approach, the image with a complete set of information is updated by implementing the subsets. From each one of the classes of subsets, projections are combined into a single subset by back projection. List mode Ordered Subset Expectation Maximization (LM-OSEM) is another class of OS-EM. It implements a list mode data format [16]. The algorithm is implemented by applying fuzzy logic. This is a better algorithm than the existing image reconstruction approaches [3]. For recursive updating method, it implements detector events instead of detector bins. The algorithm takes a long time to cover the massive amount of pixel found in the imaging system FOV, contributing to detection of coincidence event [16].

In this thesis work, the three-dimensional (3D) direct Fourier transform (FT) reconstruction technique is implemented. It uses detector coordinates in all detector tubes, where coincidences are recorded as inputs and yields the volumetric PET image as an output [43]. The algorithm starts with the creation of a multiangle sinogram and FFT. Finally, the image is formed slice by slice. The input file is produced from the GATE software and the reconstruction is implemented in a Matlab environment.

CHAPTER FOUR

METHODOLOGY

SYSTEM SPECIFICATIONS, DESIGN, AND PERFORMANCE EVALUATION OF THE PROPOSED PEM SCANNER

4.1. Overall System Design

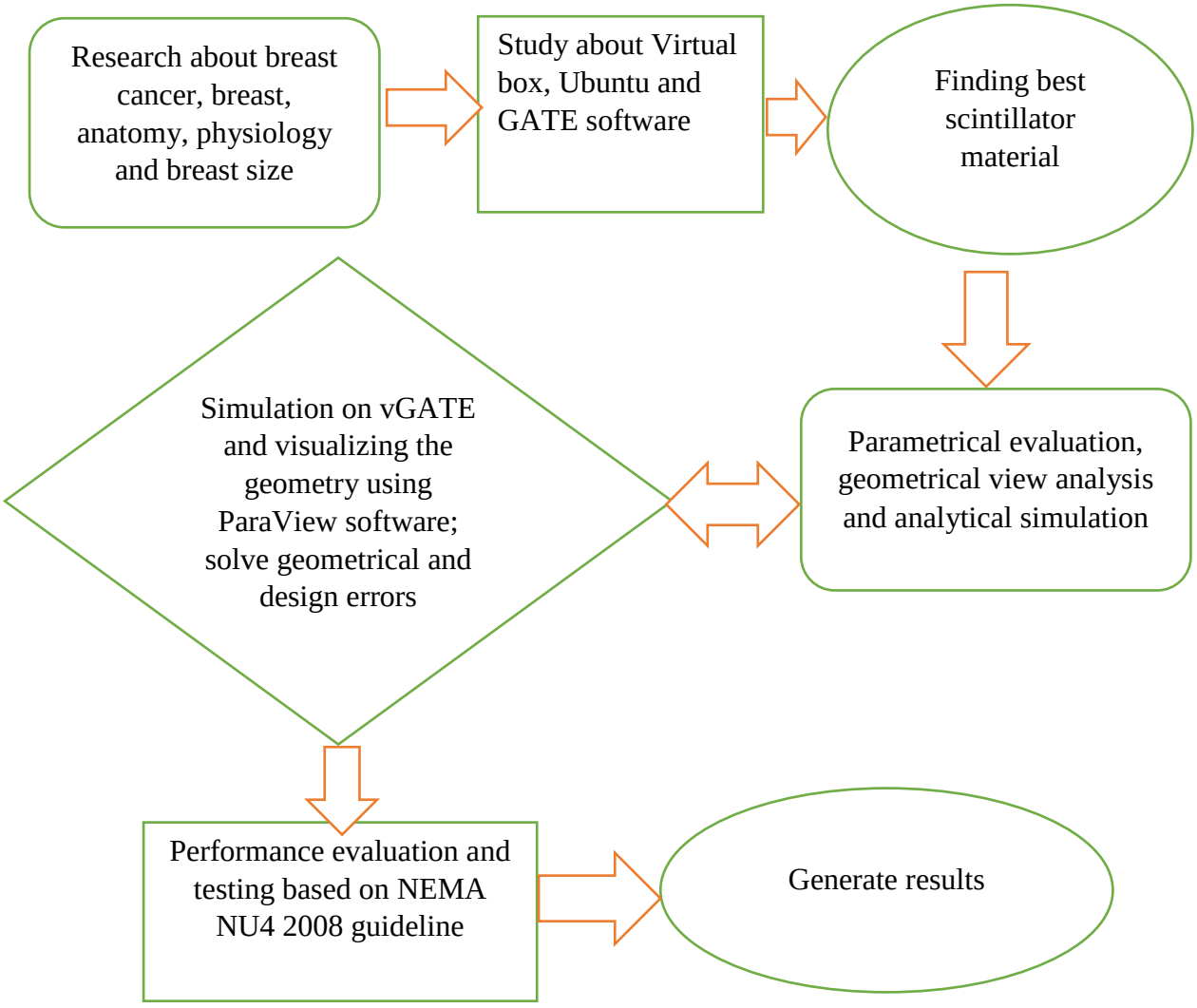

Figure 27: Schematic diagram of the flow chart of the proposed PEM scanner design.

Figure 25 presents a schematic diagram showing the flow chart of the proposed PEM scanner design including all activities required before generating the final results.

4.2. System Specifications and Design

In this study, the PEM scanner is designed and simulated for use in scanning small breast lesions at early stage. The geometrical design is done by using GATE software with different TOC scintillator crystals namely SHO, BHO, and LHO. A comparison was also done against LSO crystal. The implemented TOCs scintillators have high stopping power and good conversion efficiency compared to the existing inorganic scintillators.

The PEM scanner designed and specified in the current work has a cylindrical shape with a maximum radius of 99 mm and a minimum radius of 59 mm. It is significant enough to scan the whole parts of the breast as the breast organ is assumed to have a cylindrical shape that can fit into the gantry. The scanner has a head, module, and crystal layers. The cylinder has 39 head segments of size, 30mm x 30mm x 59mm in the x, y, and z Cartesian coordinate inside the head, respectively. The module size is 10mm x 30mm x 59mm in the x, y and directions. The module block is segmented in to a 1 x 1 x 10mm^3 crystal sizes. Table 5 presents the PEM design geometrical specifications considered for all four crystals: BHO, LHO, LSO and SHO.

Table 6: PEM design geometry specifications.

Geometry design		
Crystals		BHO, LHO, SHO and LSO
Density (g/cm3)	BHO	7.7
	LHO	8.4
	LSO	7.4
	SHO	8.1
Head		39
Module (mm)		10 X 30 X 59
Detector voxel size (mm^3)		10 X 1 X 1

Based on these geometric specifications and system architecture, the PEM design was implemented on a GATE software, has also been depicted in Fig. 28.

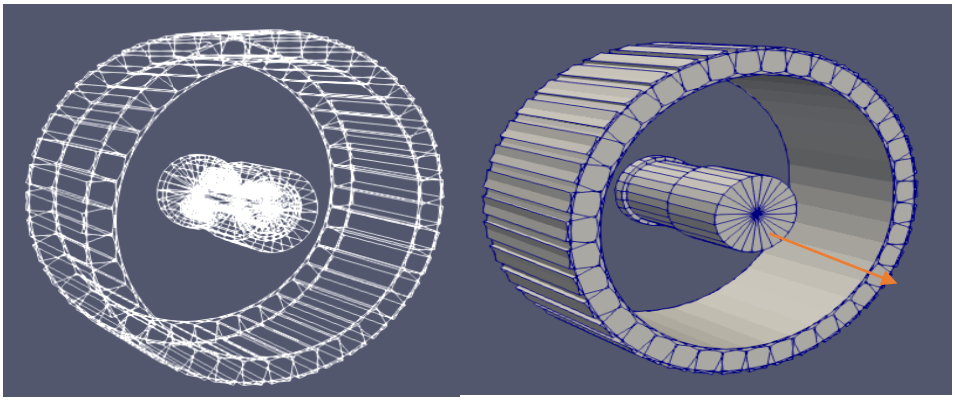

Radius = 59 mm

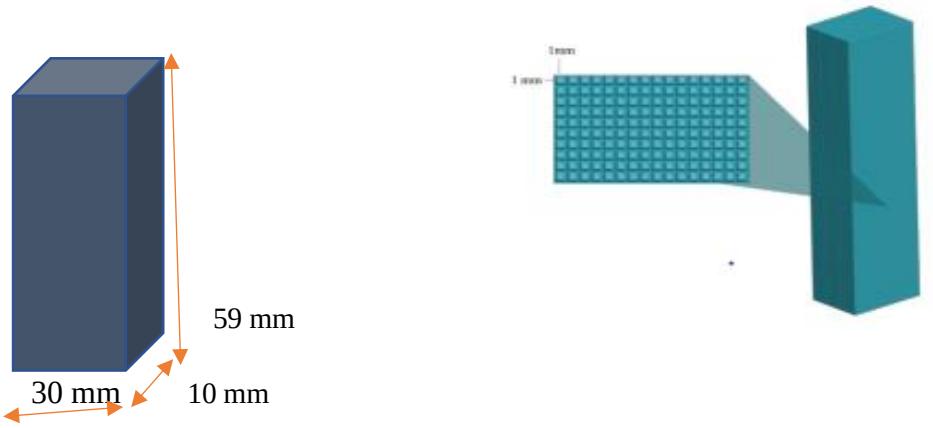

Figure 28: GATE images of the PEM. Complete scanner comprising of 39 detector modules with different views (top), Detector module (bottom left), and detector module with a pixelated section (bottom right).

The radius of the cylinder was calculated based on the average breast size while the average breast size was calculated based on equation 2. The radius is calculated accordingly based on equation 3.

In order to design the proposed PEM scanner in the current work, the mean value of the breast volume statistical data was considered. The mean volume of the left and right breast are 642 ml and 643 ml respectively. The cup size of the bra is calculated by using equation 1. The breast is assumed to be an irregular cylinder and the average volume of the left and right breast is 642.5 ml which can be calculated based on equation 2. The height and the radius of the breast are both 59 mm, calculated based on equations 3 and 4, respectively.

4.3. Monte Carlo Simulation

Nowadays, Monte Carlo simulation is an essential tool in PET and SPECT for supporting system design. Several Monte Carlo simulation software had been introduced since 1995 which are implemented in different programming tools such as C++, Matlab, python and others. Geant4 application for emission tomography (GATE) is one of the best Monte Carlo simulation software, which works based on C++ [36].

4.4. GATE

Geant4 Application for Emission Tomography (GATE), a new general purpose simulation platform for PET and SPECT applications. Is built on the Geant4 simulation toolkit for providing multiple new features [44]. The current thesis work was done based on vGATE7.2 version (open source software). It is virtual machine-dependent software, and it works by writing script on the Linux Ubuntu. GATE features include time dependent management process; user layer, application layer and developer layer incorporated with the core layer. The core layer has a base class, those are common in all Geant4- based simulations that include physics interaction and geometry construction [36]. The user layers provide a free platform for user simulation and running the simulation based on a script. The user must enter commands and build up macro files that contain collection of ordered commands. As the software is case-sensitive, the user must give the correct command. Otherwise, a lot of errors will appear. The user works on the benchmarks of the software. It contains a system, digitizer, camera, physics, source, and others. Table 7 presents the user layer descriptions found on the GATE software.

Table 7: GATE software user layer description

Name	Description
Benchmarks	They provide an example on how to use all features of GATE and experiments to simulate PET and SPECT.
System	It includes one or more rings, which contain/s the detector module. The module is blocked into scintillator blocks and segmented into crystal pixels. The geometry is designed in the ‘camera’ of the GATE platform. Simulation of realistic acquisitions can be achieved due to the synchronization of the source kinetics with the geometry. This

	includes respiratory and cardiac motion, patient movement and scanner rotation.
Digitizer	It used to simulate the electronic response of the detector within the scanner.
Camera	It is used to design the geometry of the simulation
Physics	It is used to define particles and electromagnetic processes (electromagnetic interaction of a particle with matter) for simulation purposes.
Source	Is used to define activities. The user defines the type of source, whether it is linac Beam, phase Space, Pencil Beam, TPS Pencil Beam or GPS. Many activity distributions are available on GATE. At each new event, the source manager randomly decides which source decays, and generates for it one or more primary particles [45].

4.5. Performance Evaluations

There is a standard for performance testing of PET and SPECT scanners that have been developed by National Electrical Manufacturer's Association (NEMA). The available standards include for both small animal PET and whole-body PET systems. NEMA has different versions. In the current thesis work, the NEMA NU4-2008 standard has been followed that is often used for small animal PET [30]. In order to do system performance evaluation, the size of small animals was approximated to breast size. By using this standard, different performance matrices including sensitivity, scattering fraction, spatial resolution, image quality and uniformity were computed. A summary of performance evaluation parameters of NEMA NU 4 2008 is presented in Table 8.

Table 8: Performance evaluation parameter of NEMA NU 4 2008 standard.

Performance evaluation parameter	Formula
Sensitivity	$Si = \frac{R_i - R_{B,i}}{Acal}$, $S_{A,i} = \frac{S_i}{0.9060} x100$

Scattering fraction	$SF = \frac{\sum i \sum_j C_{r+s,i,j}}{\sum i \sum_j C_{tot,i,j}}$
Spatial resolution	Set the point source image at CFOV and use DFT algorithm (in Matlab) to calculate the FWHM which dictates the spatial resolution
Image quality	By using image quality phantom of NEMA NU 4 2008
Uniformity	By using sensitivity phantom moving 10 mm away from the center of the field of view

CHAPTER FIVE

RESULTS AND DISCUSSION

5.1. Result

5.1.1. Sensitivity

The sensitivity is evaluated by NEMA NU4 2008, with 24500Bq of activities and 240 second of time varying the count rate. Sensitivity is measured at CFOV and presented in cps/Bq. Figure 29 presents the sensitivity values obtained for the four scintillator materials: LHO, BHO, LSO and SHO. Accordingly, LHO is found to have best sensitivity compared to the rest TOC scintillators with sensitivity of 0.0826cps/Bq. The next best sensitivity was found when using SHO followed by BHO while LSO offered the least performance in terms of sensitivity. The result is calculated based on equation 5.

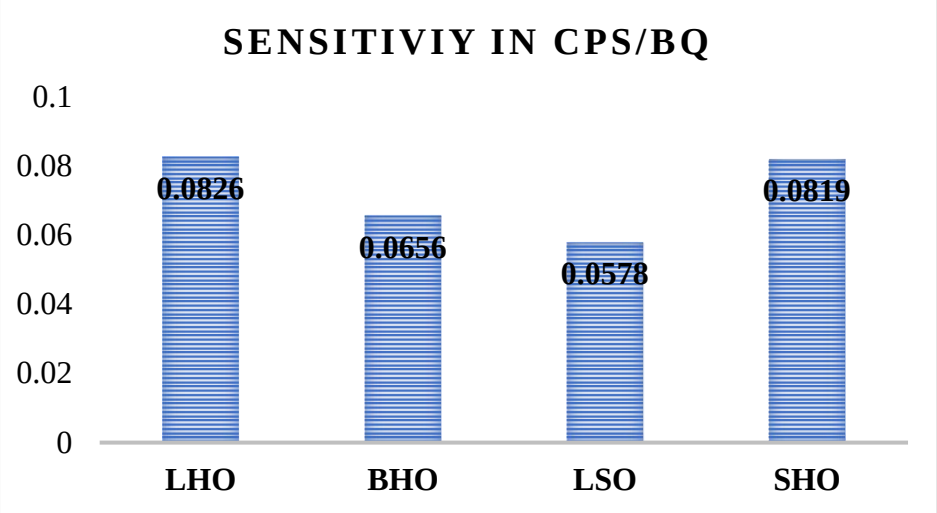

Figure 29: Sensitivity in cps/Bq.

The absolute sensitivity was also computed for all TOC scintillator materials. Once again LHO offered the best absolute sensitivity at 9.11% followed by SHO and BHO. LSO performed the least. This shows that the three TOC materials considered in the current study performed better than the reference crystal material which was LSO. It is known that LSO is one of the best scintillator materials often used in the literature when designing PET scanners. The computed sensitivity values might show that there are

other scintillator materials one can use instead of LSO when designing a PET scanner. It is calculated based on equation 6.

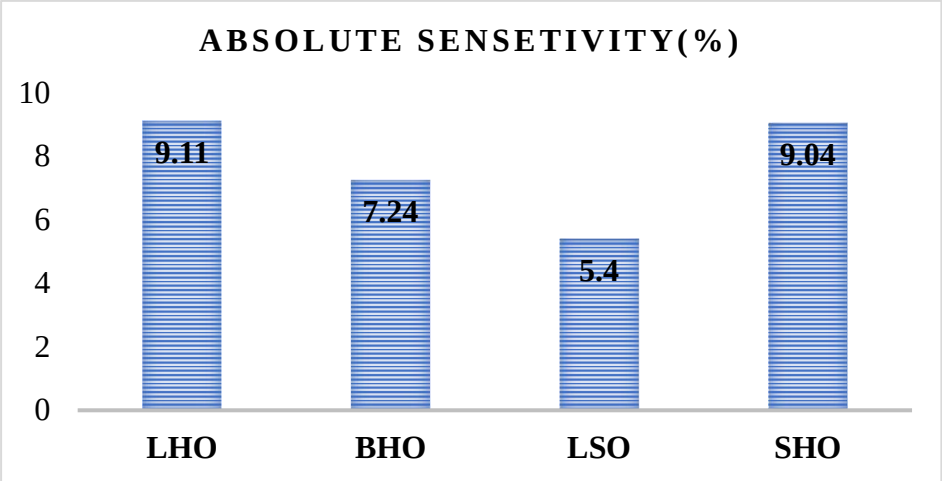

Figure 30: System absolute sensitivity for each scintillating crystal.

5.1.2. Scattering Fraction

Scatter fraction (SF) measurement follows the NEMA NU4 2008 standard [46]. The phantom dimension in NEMA NU4 2008 guideline for evaluating scattering fraction is larger than the design of the PEM detector in the current study, and some adjustments needed to be made before evaluating the SF [46]. In the design and simulation, the source radioactivity was about 24500Bq. The calculated SF of the system using different scintillator materials is presents in Table 6. The computed SF values are somehow comparable though the SF computed for BHO and LHO outperforms the other two. The percentage SF values presented in Table 6 are plotted in bar graph in Fig. 31. The result is calculated based on equation 7.

Table 9: Scattering fraction results.

Material Name	Scattering fraction	SF (%)
BHO	0.110123	11.01
LHO	0.110102	11.01
SHO	0.111972	11.19
LSO	0.111465	11.15

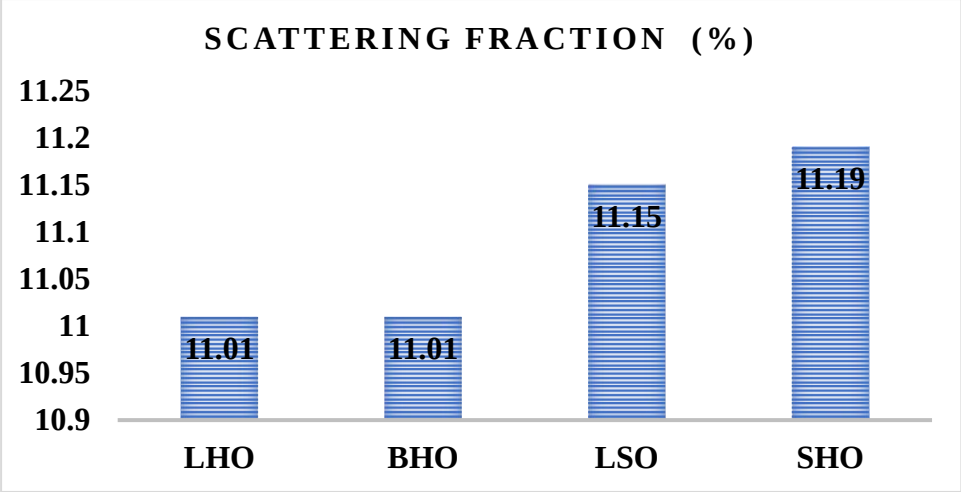

Figure 31: Scatter fraction results of the system tested using different scintillator materials.

5.1.3. Spatial Resolution

Axial measurements of the spatial resolution test results are presented in Figure 32. The figure presents a 2D slice of point source image located at CFOV, and its mean axial line profile for the LHO scintillator material which offered a spatial resolution of 1.0 mm. The average spatial resolution computed for all four scintillator materials (including the reference LSO) was 1.06 mm. Table 7 presents the spatial resolution values computed for the four scintillator materials.

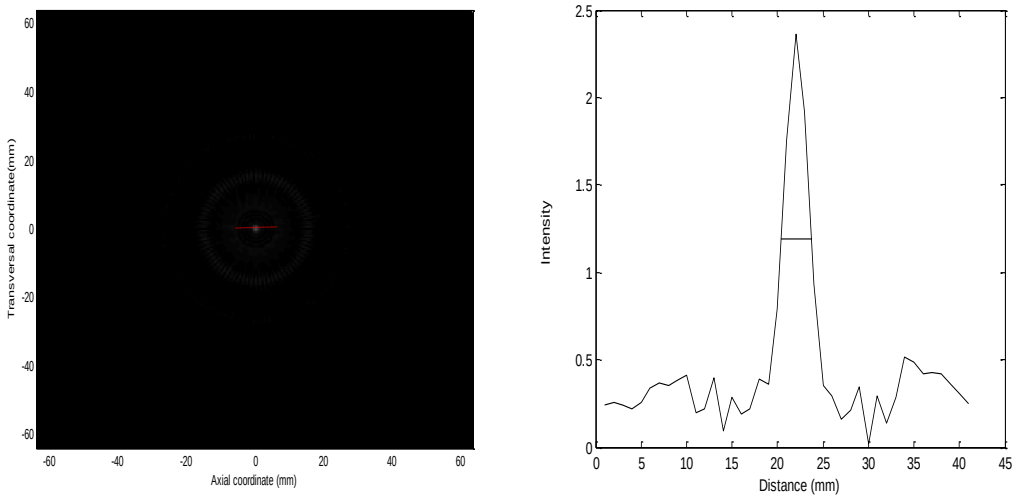

Figure 32: Point source image positioned at CFOV (left) and line profile taken axially (right).

Table 10: Spatial resolution result

Material Name	Axial spatial resolution (mm) FWHM
BHO	1.1
LHO	1.0
SHO	1.01
LSO	1.13

5.1.4. Image Quality

Figure 33 below shows the images reconstructed (using the method discussed in the previous chapter which is Fourier transform based) using the proposed PEM scanner design applied on the phantom used in the NEMA standard. As described in the previous chapter, the phantom comes in three compartments. All objects in the phantom are very well resolved with good image quality after a qualitative assessment. Figure 33 presents both the reconstructed images as well as cross sectional profiles. The total number of slices was 512 and the three reconstructed images shown in Fig. 33 represent slices numbers 314, 240, and 221 respectively. For the slices considered in the first and last compartments, horizontal cross sections are depicted while for the middle compartment that contains the five rods, an oblique cross section is depicted that passes through the larger rod. The image quality results presented in Fig. 33 are only for the LHO scintillator while the results for the other three scintillators are qualitatively similar.

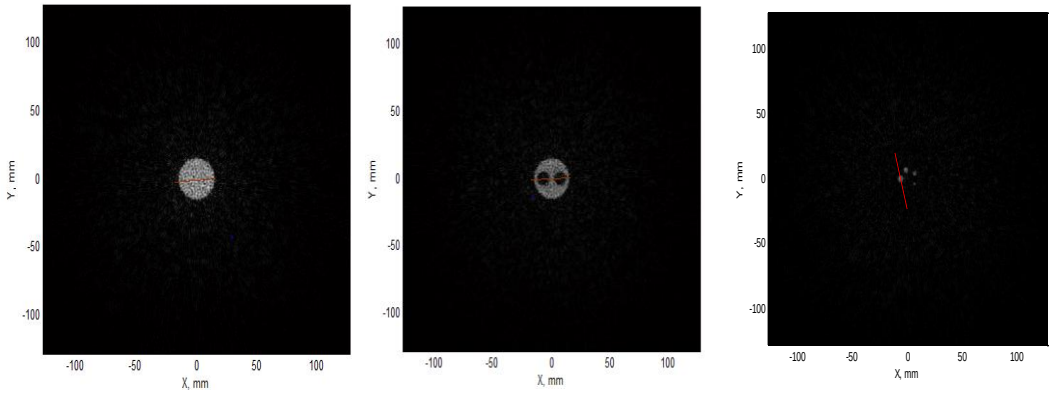

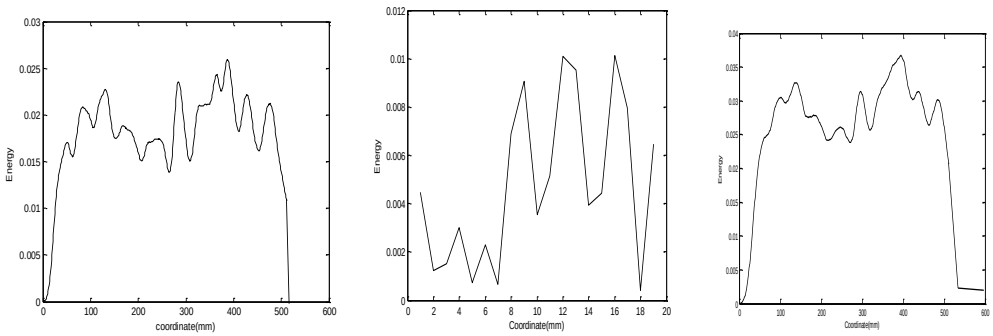

Figure 33: Reconstructed images at three slice positions that indicate a unform region, two chambers filled with air and water and five ^{18}F filled rods respectively, using the NEMA image quality phantom (top), corresponding cross-sectional profiles (bottom).

5.1.5. Uniformity

Figure 34 presents the uniformity profiles computed for the three scintillators considered in the current study. Generally, the system is found to be uniform across the sensitivity tests which are performed at different axial locations measured at the centre and every 10 mm distance away from the centre.

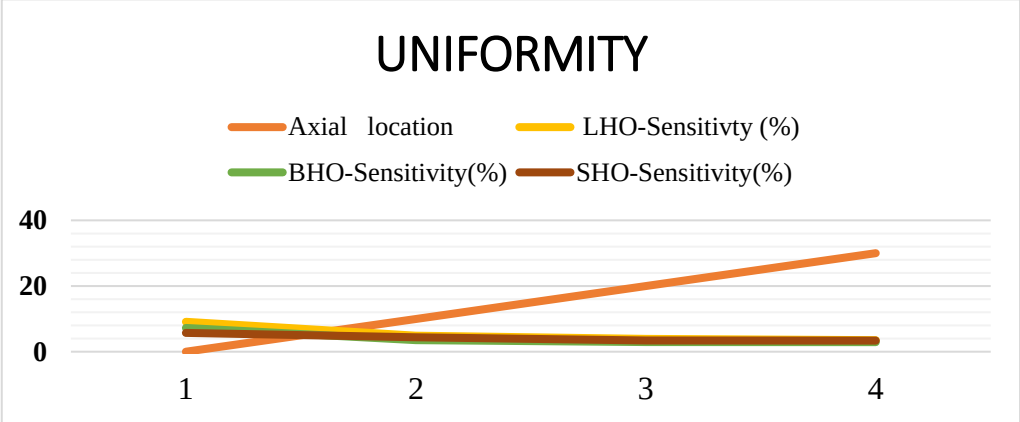

Figure 34: Uniformity computed at different locations in steps of 10 mm away from the centre using the sensitivity phantom.

5.2. Discussion

The spatial resolution test measures axially and the average spatial resolution for the suggested BHO, LHO, SHO and LSO scintillators is 1.06mm measured at FWHM. The measured spatial resolution is better than the resolution values reported previously in other researches as well as commercially available PEM scanners. Table 8 compares the spatial resolution values reported using previously proposed methods against the

proposed approach in the current study. The comparison was done applying the same testing procedures. All the methods proposed previously in years 2006, 2014, 2015 and 2018 resulted in axial resolution inferior to the proposed method except the one proposed by Musa et al. which offered an axial resolution similar to the proposed method in the current work.

Table 11: Descriptive comparison of spatial resolution test results between existing methods and the method proposed in the current study.

Scanners	Spatial Resolution	Method
Proposed PEM	Axial = 1 mm	Proposed method (2022)
Musa PEM Scanner	Axial = 1 mm	Musa et al. (2018)
PEMi	Axial = 1.4 mm	Lin et al. (2015)
G-PET	Axial = 5.0 mm	Karp et al (2014)
Li-PET	Axial = 2.7 mm	Li et al. (2006)

Comparison was also done in terms of absolute sensitivity of the system reported before against the proposed method. A best sensitivity of 9.11% (when LHO was used as a scintillator) was obtained using the proposed method much superior to the other two systems proposed: PEMI and G-PET. While the system proposed by Li et al. (Li-PET) resulted in an absolute sensitivity value which was slightly higher than the proposed scheme, the method proposed by Musa et al. (Musa-PEM) offered the best absolute sensitivity. Figure 35 presents this absolute sensitivity values for the different systems.

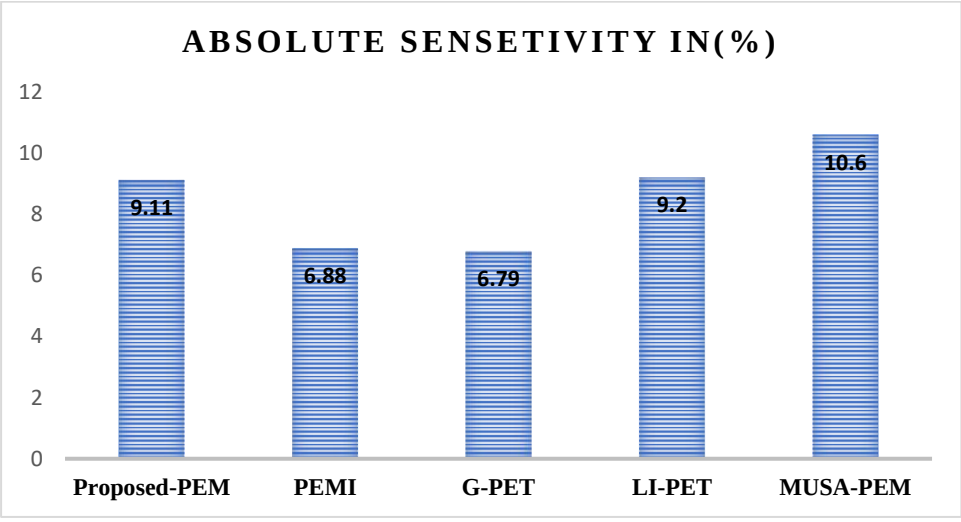

Figure 35: Comparison of absolute sensitivity.

Table 9 presents comparison between different scanners in terms of a scattering fraction parameter. The proposed method was compared to previously proposed methods in terms of the scatter fraction. However, not all of the studies reported the scattering fraction values that resulted from using their proposed scanners. Compared to G-PET and PEMi scanners, the proposed PEM scanner in the current study offered the best scattering fraction, showing its great promises.

Table 12: Comparison of scattering fractions computed for different scanners.

PEM /PET scanners	Scatter fraction (%)	Energy window (Kev)
G-PET	39	410-665
Proposed - PEM	11	350-650
Musa PEM Scanner	---	---
PEMi	43.5	360-660
Li-PET	---	---

CHAPTER SIX

CONCLUSIONS AND RECOMMENDATIONS

6.1. Conclusion

The proposed PEM simulator design achieved commendable results based on measures commonly used to test the efficiency of such scanners. The design was fundamentally based on the GATE simulation software. The sensitivity, spatial resolution, scatter fraction, uniformity, and image quality are checked using NEMA NU4 -2008 standards of small animal PET testing procedure. The geometrical design of the scanner is simulated to assume a cylindrical shape to follow the shape of the breast. The detector is configured in such a way that it is made of a cylindrical ring to cover whole parts of the breast. This is the best geometry to scan and detect small lesions at early stage.

The proposed method fairly passed all of the tests that are often employed the efficiency of a given PEM scanner. The computed spatial resolution, sensitivity, scatter fraction, uniformity, and image quality are all assessed to be promising compared to existing PEM scanner designs. The method attained an excellent spatial resolution of 1mm according to NEMA NU4 - 2008. This study shows that the PEM scanner is capable of achieving higher spatial resolution and sensitivity at low cost. This clearly shows the feasibility of using the three scintillator materials used: LHO, SHO and BHO for cost effective PEM design and development.

6.2. Recommendations

There are still rooms to improve the performance of the PEM scanner design proposed in the current study. Future studies on alternative crystals and Nano-material based scintillator other than the ones used in the current study might improve the system sensitivity and spatial resolution of the PEM scanner. Instead of focusing on the axial resolution, the radial and tangential resolutions obtained by the system might also be interesting to test the efficiency of the system.

One could think of using different techniques during image reconstruction which might further affect the quality of the reconstructed image at the end of the day. It is only Fourier transform method that is considered in the current study while their other

interesting image reconstruction methods available in the literature for someone to exploit. Also, after image reconstruction, different methods could be checked for their efficiency in getting rid of the artifacts that may still be present. Such artifacts were also present in some of the results presented in the current work as demonstration. Dealing with such and similar other issues was beyond the scope of the current study and that might require much further investigation.

REFERENCES

[1] "Understanding a Breast Cancer Diagnosis, American Cancer Society. [Online];".

[2] "https://acsjournals.onlinelibrary.wiley.com/doi/full/10.3322/caac.21660)".

[3] D. M. S. Musa, "Simulation and evaluation of high performance cost effective positron emission mammography scanner," *Journal of Instrumentation,* vol. 13, Nov 2018.

[4] S. R., "Breast cancer burden in Africa: evidence from GLOBOCAN 2018.," pp. 763-771..

[5] WHO, "National cancer control plan of Ethiopia," Globocan 2020.

[6] D. M. ,. T. D. Bailey, "Positron Emission Tomography," *London: Springer-Verlag,* 2005.

[7] T. G. Turkington, "Introduction to PET instrumentation," vol. 29, pp. 1-8, 2001.

[8] e. a. Lin., "Performance evaluation and initial clinical test of the PEMI system," vol. 62, p. 5, Oct. 2015..

[9] S. J. L. E. B. J. Bushberg JT, "The Essential Physics of Medical Imaging, ed 3, Chapters 12 and 13," *Lippincott Williams & Wilkins,* Philadelphia, PA, 2012.

[10] S. R. Cherry, " Physics of Nuclear Medicine," 2012.

[11] E. Mikhaylova, Simulation of the expected performance of seamless scanner for brain PET Based on High pixlated CdTe detector, vol. 33, Feb. 2014., pp. 332-339.

[12] C. a. J. T. S. A. Karimian, "CYBPET: a cylindrical PET system for breast imaging," Vols. 1-2, pp. 427-435, 2005.

[13] Li., "Developed high resolution PET camera for the purpose brain and breast studies," 2006.

[14] Karp, "design of high-resolution and a high sensitivity brain PET scanner called G-PET," 2014.

[15] C. J. Thompson, " Feasibility study for positron emission mammography," April 1994.

[16] M. L. G. a. M. Kolstein, "Evaluation of Origin Ensemble algorithm for image reconstruction for pixelated solid state detectors with large number of channels," 2013.

[17] Wikiwand, “Avalanches in proportional counters,” 2017.

[18] k. G., “Radiation detection and measurement,” 2010.

[19] S. Charry, “physics in nuclear mdicine,” 2004.

[20] T. a. W. S. Takahashi, “Recent progress in CdTe and CdZnTe detectors,” *IEEE Transaction on Nuclear Sciences,* vol. XX(Y), p. 101, 2000.

[21] M. Nikl, “Scintillation detectors for X-rays. Measurement Science and technology,” vol. 17(4), 2006.

[22] A. W. A. &. B. E. Lempicki, “Fundamental limits of scintillator performance. Nuclear Instruments And Methods In Physics Research Section A: Accelerators Spectrometers, Detectors And Associated Equipment,,” pp. 304-311.

[23] L. S. R. V. Venkataramani V.S, “Cerium-doped alkaline-earth Hafnium oxide scintillators having Improved transparency and Method of making the same”.

[24] a. W. M. Edgar Van Loaf, “Scintillation properties of SrHfO3 : Ce3+ and BaHfO3 : Ce3+ ceramics,” vol. 54, no. 3, pp. 741 - 743, 2007.

[25] C. F. a. M. Woody, “Fast Dense Low cost Scintillator for Nuclear Physics,” 31 07 2009.

[26] H. L. a. O. G. XiChen, “Terbium-doped LiYbF4 nanomaterial-based scintillator responding to X-rays with high-resolution imaging applications,” *CrystEngCOM,* vol. 1, no. 14 2022, 11 Mar 2022.

[27] D. E. M. a. J. R, “Breast volume and bra size,” October 2010.

[28] J. W. &. Scurr, “Evaluation of professional bra fitting criteria for bra selection and fitting in the UK,” vol. 55, no. 6, pp. 704-71, 2012.

[29] E. G. 7. P. T. F. Students, Gread 7 physics txetbook, vol. 1.0, NEAEA, Ed., Addis abeba: MoE, Ethiopia, June 15, 2020.

[30] N. S. Publication, “Performance Measurements of Small Animal Positron Emission Tomographs,” 2008.

[31] N. (National electrical manufacurerassociation), “NEMA NU 4 2008 , performance and measurments ofsmall animal positron emission mamography,” vol. 1, pp. 4- 19, 2008.

[32] a. C. L. Cassen B, “Instrumentation for 131I use in medical studies,” *Nucleonics 9:46- 50,* 1951.

[33] W. S. Blumgart HL, “Studies on the velocity of blood flow,” vol. 4:, pp. 15-31, 1927.

[34] L. M. Lawrence EO, “he production of high-speed light ions without the use of high voltages,” *Phys Rev 40:19-30,,* 1932.

[35] H. G, “Radioelements as tracers in physics and chemistry,” *Chem News 108:166,* 1913.

[36] “Monte Carlo simulations in emission tomography and GATE,” *Nuclear Instruments and Methods in Physics Research,* p. 250–303, 2003.

[37] “Cyclotron Produced Radionuclides: Principles and Practice,” IAEA VIENNA, 2008.

[38] e. a. Joanna., “PET and Drug Research and Developmen,” Mar. 1999.

[39] T. D. B. T. Beyer T, “A combined PET/CT scanner for clinical oncology,” pp. J Nucl Med 41:1369-1379, 2000.

[40] L. A. J. R. Cherry SR, “The integration of positron emission tomography with magnetic resonance imaging,” pp. 416-438, 2000.

[41] e. a. Wendie., “High-Resolution Fluorodeoxyglucose Positron Emission Tomography with Compression (“Positron Emission Mammography,” 17 July 2006.

[42] R. E. a. Schmiz, “the physics of PET/CT scanners”.

[43] U. O. P. M. M. a. G. M. Ozsahin D, “Simulation of novel scintillator crystals for brain PET,” *Ozsahin et al 2020 JINST 15 C05024,* vol. 1, p. 14, May 11 2020.

[44] D.Strulab∗G.SantincaD.LazarodaV.BretondaC.Morelba, “GATE GATE (geant4 application for tomographic emission): a PET/SPECT general-purpose simulation platform,” vol. 125, pp. 75-79, eptember 2003,.

[45] GATE, “virtual GATE guide line,” vol. 7.2.

[46] C. C. A. a. J. G. P. Moliner, “Time reconstruction study using tubes of response backprojectors in list mode algorithms applied to a monolithic crystals based breast PET", Nuclear Science Symposium and Medical Imaging Conference (NSS/MIC,” pp. 1-5, 2013.

[47] J. J. V. &. P. Kinahan, “PET:current challange and opportunities for technological advances in clinical and pre clinical imageing system,” vol. 17, pp. 385-414, 2015.

[48] M. P. a. K. M. V. Zhang J, “Performance evaluation of the next generation solid state digital photon counting PET/CT image,” *JNMMI Res,* vol. 8, Nov. 6 2018.

[49] J. S. Karp, “Benefits of time of fight in PET: expermental and clinical report,” vol. 49, Mar. 2008, pp. 462-470.

[50] P. A. a. C. Lois, “Analytical Study of the Effect of the System Geometry on Photon Sensitivity and Depth of Interaction of Positron Emission Mammography,” *Journal of Oncology,* 2012.

[51] I. T. o. N. Science, “Development of Pr:LuAG Scintillator Array and Assembly for Positron Emission Mammography,” vol. 57, no. 3, p. 1492 – 1495, June 2010.

[52] “Medical Imaging Conference and Room-Temperature Semiconductor Detector Workshop (NSS/MIC/RTSD),” in *IEEE Nuclear Science Symposium,* 29 Oct.-6 Nov. 2016.

[53] Junwei, “properties of scintillator crystal,” 2009.

[54] Michael, “ceramic doped scintillators and thier characterisation,” 2009 .

[55] Bristol, “A Century of X-Rays and Radioactivity in Medicine,” 1993.

[56] T. DW, “Multimodality imaging of structure and function,” *Phys Med Biol 53:R1-R39,* 2008.

[57] D. E. M. a. J. R., “Breast volume and bra size, Steele Biomechanics Research Laboratory,” March 2011.

[58] F. Bouman, “volumetric measurement of the breast before and during mammaplasty,” vol. 23, no. 3, pp. 263-4, 1970.

[59] N. B. E. a. S. S. Bulstrode, “Breast volume assessment: comparing five different techniques,” *The Breast Journal,,* vol. 10, pp. 117-23, 2001.

[60] I. B. a. D. Lazaro1, “Nuclear Instruments and Methods in Physics Research Section A: Accelerators, Spectrometers, Detectors and Associated Equipme,” *Monte Carlo simulations in emission tomography and GATE,* vol. 569, no. 2, pp. 323-329, 20,December 2006.

[61] T. Yanagida, “devlopment of Pr:LuAG Scintillator Array and Assembly for Positron Emission Mammography,” 2010.

[62] “Scintillation detector comprising a scintillation material coupled to a photomultiplier tube,” *scintillator matrial group,* 2013.

[63] “Spatial resolution of the PET system,” *BMJ. 2003,* Jun 2008.

[64] R. a. Busemann-Sokole, “Computers in Nuclear Medicine,” January 1985.

[65] S. a. A. A. Tong, “Image reconstruction for PET/CT scanners:past achievements and future challenges,” pp. 529-545.

Appendix

Camera

```
#       CYLINDRICAL
/gate/world/daughters/name cylindricalPET
/gate/world/daughters/insert cylinder
/gate/cylindricalPET/placement/setTranslation 0.0 0.0 0.0 cm
/gate/cylindricalPET/geometry/setRmax   99.0 mm
/gate/cylindricalPET/geometry/setRmin   59.0 mm
/gate/cylindricalPET/geometry/setHeight 59.0 mm
/gate/cylindricalPET/setMaterial Air
/gate/cylindricalPET/vis/forceWireframe
/gate/cylindricalPET/vis/setColor white
/gate/cylindricalPET/vis/setVisible 0
#       HEAD
/gate/cylindricalPET/daughters/name head
/gate/cylindricalPET/daughters/insert box
/gate/head/placement/setTranslation 74.0 0.0 0.0 mm
/gate/head/geometry/setXLength  30.0 mm
/gate/head/geometry/setYLength  30.0 mm
/gate/head/geometry/setZLength 59.0 mm
/gate/head/setMaterial Air
/gate/head/vis/setColor blue
/gate/head/vis/setVisible 0
#       END-SHIELDING
#/gate/head/daughters/name endshielding
#/gate/head/daughters/insert box
#/gate/endshielding/placement/setTranslation 0.0 0.0 0.0 cm
#/gate/endshielding/geometry/setXLength 8.0 cm
#/gate/endshielding/geometry/setYLength 32.0 cm
#/gate/endshielding/geometry/setZLength 1.0 mm
#/gate/endshielding/setMaterial Lead
```

```
#/gate/endshielding/repeaters/insert cubicArray
#/gate/endshielding/cubicArray/setRepeatNumberX 1
#/gate/endshielding/cubicArray/setRepeatNumberY 1
#/gate/endshielding/cubicArray/setRepeatNumberZ 2
#/gate/endshielding/cubicArray/setRepeatVector 0.0 0.0 40.1 cm
#/gate/endshielding/vis/setColor white
#       SEPTA
#/gate/head/daughters/name septa
#/gate/head/daughters/insert box
#/gate/septa/placement/setTranslation -1.5 0.0 0.0 cm
#/gate/septa/geometry/setXLength 5.0 cm
#/gate/septa/geometry/setYLength 32.0 cm
#/gate/septa/geometry/setZLength .5 mm
#/gate/septa/setMaterial Tungsten
#/gate/septa/repeaters/insert cubicArray
#/gate/septa/cubicArray/setRepeatNumberX 1
#/gate/septa/cubicArray/setRepeatNumberY 1
#/gate/septa/cubicArray/setRepeatNumberZ 3
#/gate/septa/cubicArray/setRepeatVector 0.0 0.0 10.0 mm
#/gate/septa/vis/setColor blue
#       MODULE
/gate/head/daughters/name module
/gate/head/daughters/insert box
/gate/module/placement/setTranslation -10.0 0.0 0.0 mm
/gate/module/geometry/setXLength 10.0 mm
/gate/module/geometry/setYLength 30.0 mm
/gate/module/geometry/setZLength 59.0 mm
/gate/module/setMaterial Air
/gate/module/vis/setColor blue
/gate/module/vis/setVisible 1
#       BLOCK
#/gate/module/daughters/name block
```

```
#/gate/module/daughters/insert box
#/gate/block/placement/setTranslation 0.0 0.0 0.0 cm
#/gate/block/geometry/setXLength 30 mm
#/gate/block/geometry/setYLength 15.9 mm
#/gate/block/geometry/setZLength 19.9 mm
#/gate/block/setMaterial Air
#/gate/block/vis/setVisible 0
#       C R Y S T A L
/gate/module/daughters/name crystal
/gate/module/daughters/insert box
/gate/crystal/placement/setTranslation 0.0 0.0 0.0 cm
/gate/crystal/geometry/setXLength 10.0 mm
/gate/crystal/geometry/setYLength 1.0 mm
/gate/crystal/geometry/setZLength 1.0 mm
/gate/crystal/setMaterial Air
/gate/crystal/vis/setVisible 0
#       LSO layer
/gate/crystal/daughters/name LSO
/gate/crystal/daughters/insert box
/gate/LSO/placement/setTranslation 0.0 0.0 0.0 mm
/gate/LSO/geometry/setXLength 10.0 mm
/gate/LSO/geometry/setYLength 1.0 mm
/gate/LSO/geometry/setZLength 1.0 mm
/gate/LSO/setMaterial           LHO
/gate/LSO/vis/setColor green
/gate/LSO/vis/setVisible 0
#       BGO layer
#/gate/crystal/daughters/name BGO
#/gate/crystal/daughters/insert box
#/gate/BGO/placement/setTranslation +0.75 0.0 0.0 cm
#/gate/BGO/geometry/setXLength 1.5 cm
#/gate/BGO/geometry/setYLength 3.0 mm
```

```
#/gate/BGO/geometry/setZLength 3.8 mm
#/gate/BGO/setMaterial BGO
#/gate/BGO/vis/setColor yellow
#         R E P E A T    C R Y S T A L
/gate/crystal/repeaters/insert cubicArray
/gate/crystal/cubicArray/setRepeatNumberX 1
/gate/crystal/cubicArray/setRepeatNumberY 30
/gate/crystal/cubicArray/setRepeatNumberZ 59
/gate/crystal/cubicArray/setRepeatVector 0.0 1.0 1.0 mm
#         R E P E A T    BLOCK
#/gate/block/repeaters/insert cubicArray
#/gate/block/cubicArray/setRepeatNumberX 1
#/gate/block/cubicArray/setRepeatNumberY 30
#/gate/block/cubicArray/setRepeatNumberZ 250
#/gate/block/cubicArray/setRepeatVector 0.0 1.0 1.0 mm
#         R E P E A T MODULE
/gate/module/repeaters/insert cubicArray
/gate/module/cubicArray/setRepeatNumberX 1
/gate/module/cubicArray/setRepeatNumberY 1
/gate/module/cubicArray/setRepeatNumberZ 1
/gate/module/cubicArray/setRepeatVector 0.0 0.0 0.0 mm
#         R E P E A T HEAD
/gate/head/repeaters/insert ring
/gate/head/ring/setRepeatNumber 30
/gate/cylindricalPET/moves/insert orbiting
/gate/cylindricalPET/orbiting/setSpeed .1875 deg/s
/gate/cylindricalPET/orbiting/setPoint1 0 0 0 cm
/gate/cylindricalPET/orbiting/setPoint2 0 0 1 cm
#         A T T A C H    S Y S T E M
/gate/systems/cylindricalPET/rsector/attach head
/gate/systems/cylindricalPET/module/attach module
#/gate/systems/cylindricalPET/submodule/attach block
```

```
/gate/systems/cylindricalPET/crystal/attach crystal
/gate/systems/cylindricalPET/layer0/attach LSO
#/gate/systems/cylindricalPET/layer1/attach BGO
#         A T T A C H    C R Y S T A L  SD
/gate/LSO/attachCrystalSD
#/gate/BGO/attachCrystalSD
/gate/systems/cylindricalPET/describe
```

Phantom

```
 #         P H A N T O M
/gate/world/daughters/name AcrylicCube
/gate/world/daughters/insert box
/gate/AcrylicCube/setMaterial Plexiglass
/gate/AcrylicCube/geometry/setXLength  10. mm
/gate/AcrylicCube/geometry/setYLength  10. mm
/gate/AcrylicCube/geometry/setZLength  10. mm
/gate/AcrylicCube/placement/setTranslation 0.0 0.0 0.0 mm
/gate/AcrylicCube/vis/forceSolid
/gate/AcrylicCube/vis/setColor red
/gate/AcrylicCube/attachPhantomSD
#/gate/endshielding/attachPhantomSD
#/gate/septa/attachPhantomSD
```

Source

```
##################
#                  #
#    S O U R C E   #
#                  #
##################
#/gate/source/addSource twogamma
#/gate/source/twogamma/setActivity 1000. becquerel
#/gate/source/twogamma/gps/particle gamma
#/gate/source/twogamma/setType backtoback
```

```
#/gate/source/twogamma/gps/energytype Mono
#/gate/source/twogamma/gps/monoenergy 511. keV
#/gate/source/twogamma/gps/centre 0.0 0.0 0.0 cm
#/gate/source/twogamma/gps/angtype iso
/gate/source/addSource F18LineSource
/gate/source/F18LineSource/setActivity 100. becquerel
/gate/source/F18LineSource/gps/particle e+
/gate/source/F18LineSource/setForcedUnstableFlag true
/gate/source/F18LineSource/setForcedHalfLife 6586.2 s
/gate/source/F18LineSource/gps/energytype Fluor18
/gate/source/F18LineSource/gps/type Volume
/gate/source/F18LineSource/gps/shape Cylinder
/gate/source/F18LineSource/gps/radius .5 mm
/gate/source/F18LineSource/gps/halfz 34.0 mm
/gate/source/F18LineSource/gps/angtype iso
/gate/source/F18LineSource/gps/centre 0. 0.0 0. mm
#/gate/source/addSource O15LineSource
#/gate/source/O15LineSource/setActivity 1. becquerel
#/gate/source/O15LineSource/gps/particle e+
#/gate/source/O15LineSource/setForcedUnstableFlag true
#/gate/source/O15LineSource/setForcedHalfLife 122.24 s
#/gate/source/O15LineSource/gps/energytype Oxygen15
#/gate/source/O15LineSource/gps/type Volume
#/gate/source/O15LineSource/gps/shape Cylinder
#/gate/source/O15LineSource/gps/radius .5 mm
#/gate/source/O15LineSource/gps/halfz 34.0 mm
#/gate/source/O15LineSource/gps/angtype iso
#/gate/source/O15LineSource/gps/centre 0. 0.0 0. mm
#/gate/source/addSource Na22
#/gate/source/Na22/setActivity 1000  Bq
#/gate/source/Na22/gps/particle ion
#/gate/source/Na22/gps/ion 11 22 0 0
```

```
#/gate/source/Na22/gps/monoenergy 0. keV
#/gate/source/Na22/gps/type Plane
#/gate/source/Na22/gps/shape Circle
#/gate/source/Na22/gps/radius 0.3 mm
#/gate/source/Na22/gps/angtype iso
#/gate/source/Na22/gps/centre 0.0 0.0 0.0 mm
#/gate/source/Na22/setForcedHalfLife 82078747.2 s
#/gate/source/Na22/setForcedUnstableFlag true
#/gate/source/Na22PointSource/setForcedUnstableFlag true
#/gate/source/Na22PointSource/HalfLife
#/gate/source/Na22PointSource/gps/energytype Sodium22
/gate/source/list
```

MY PET

```
/vis/disable
#/control/execute MYVISU.mac
/gate/geometry/setMaterialDatabase ../../GateMaterials.db
#     W O R L D
/gate/world/geometry/setXLength 140. cm
/gate/world/geometry/setYLength 140. cm
/gate/world/geometry/setZLength 140. cm
/gate/world/vis/setVisible 0
/control/execute MYCAMERA.mac
/control/execute MYPHANTOM.mac
/control/execute MYPHYSICS.mac
#         I N I T I A L I Z E
/gate/run/initialize
/control/execute MYDIGITIZER.mac
#         S O U R C E
/control/execute sources.mac
#         V E R B O S I T Y
#/gate/verbose Physic    0
```

```
#/gate/verbose Cuts      0
#/gate/verbose Actor     0
#/gate/verbose SD        0
#/gate/verbose Actions   0
#/gate/verbose Step      0
#/gate/verbose Error     0
#/gate/verbose Warning   0
#/gate/verbose Output    0
#/gate/verbose Core      0
/run/verbose 0
/event/verbose 0
/tracking/verbose 0
#          O U T P U T
/gate/output/root/enable
/gate/output/root/setFileName benchPET
/gate/output/root/setRootHitFlag 0
/gate/output/root/setRootSinglesFlag 1
/gate/output/root/setRootCoincidencesFlag 1
/gate/output/root/setSaveRndmFlag 1
#/gate/output/root/setRootdelayFlag 1
#enabling sinogram
#/gate/output/sinogram/enable
#/gate/output/sinogram/setFileName MySinogramFileName
#/gate/output/sinogram/RadialBins 256
#   R A N D O M
#JamesRandom Ranlux64 MersenneTwister
/gate/random/setEngineName MersenneTwister
#/gate/random/setEngineSeed default
#/gate/random/setEngineSeed auto
/gate/random/setEngineSeed 123456789
#/gate/random/resetEngineFrom fileName
/gate/random/verbose 1
```

```
#         S T A R T
/gate/application/setTimeSlice     1. s
/gate/application/setTimeStart     0. s
/gate/application/setTimeStop      20. s
/gate/application/startDAQ
#plotter
/gate/output/plotter/enable
/gate/output/plotter/showPlotter
/gate/output/plotter/setNColumns 2
/gate/output/plotter/setPlotHeight 250
/gate/output/plotter/setPlotWidth 300
/gate/output/plotter/addPlot hist Ion_decay_time_s
/gate/output/plotter/addPlot hist Positron_Kinetic_Energy_MeV
/gate/output/plotter/addPlot tree Singles comptonPhantom
/gate/output/plotter/addPlot tree Coincidences energy1
/gate/output/plotter/listPlots
```

Matlab code

Create coin-file

```
%we create mat-file, containing the coordinates of det.1 and det.2 centers,
%where det.1 and det.2 is the pair of detectors with a coincidence
%!this script is specially for multiple source files "resolution"
close all
file_group_name = 'Image quality_LHOCoincidences_3'; %CHANGE THIS STRING ACCORDING TO FILE NAME(S)
Kfiles = 2; %SET ACCORDING TO THE NUMBER OF SOURCE FILES
%some assumed constants (!!! always check !!!)
Rcoil = 64; %mm, radius of detector coil (center)
dz = 1; %mm, layer thickness
Nrings = 59;5
Nrsec = 39;
Ncrrow =30; %number of crystals in one row of an r-sector
```

```
Kcoin = 0;

Xcdet1meter = [];

Ycdet1meter = [];

Zcdet1meter = [];

Xcdet2meter = [];

Ycdet2meter = [];

Zcdet2meter = [];
```

Image Reconstruction

```
%image reconstruction from GATE simulated data

close all

%!all units in SI

fileid = 'Image quality_LHOCoincidences_3'; %SET APPROPRIATE MAT-FILE NAME (from CoincidenceMatFiles folder)

create_sinograms_flag = 1;

process_sinogram_flag = 1;

%imaging parameters

dr = 1e-3; %nominal spatial resolution (in meters)

Nxy = 128; %number of resolution cells in transversal dimensions

Nz = 128; %number of resolution cells in axial dimension

Pdecim = 2; %number of subarrays along each dimension of slice - to avoid overwriting at resampling stage (4 should be more than enough)

Jhalf = 1; %how many samples each side from the central are included in resampling (even 1 might be OK)

%gantry parameters (!!! SHOULD CORRESPOND TO WHAT WE HAVE IN SIMULATION!!!)

Rcoil = 0.064; %radius of detector coil (center)

H = 0.059; %height of gantry

%computed parameters and some arrays

Lxy = Nxy*dr; %image linear horizontal size

Lz = Nz*dr; %image linear vertical size

dtheta = 2*dr / Lxy; %angle pitch providing sufficient sampling

Mtheta = round(pi/dtheta); %to create uniform grid of projection angles

dtheta = pi/Mtheta; %recompute pitch for uniformity
```

```
thetavec = dtheta * (0 : Mtheta-1) - pi/2;

gammamax = atan(0.5*H/Rcoil); %SET CAREFULLY: 0.5 - all possible LoRs registered, 0.25 - half of them, but invariant point spread function

dgamma = 2*dr / Lz; %angle pitch providing sufficient sampling (can be increased if too many computations)

Mgamma = round(2*gammamax/dgamma); %to create uniform grid of projection angles

gammavec = dgamma * (-Mgamma/2+0.5 : Mgamma/2-0.5);

if create_sinograms_flag

  %determine 4 parameters for each LoR

load(['CoincidenceMatFiles/' fileid '.mat']);

[scoin, vcoin, thetacoin, gammacoin] = RestoreSinoPars(Xcdet1meter, Ycdet1meter, Zcdet1meter, Xcdet2meter, Ycdet2meter, Zcdet2meter);

  for m = 1:Mgamma

    [m Mgamma]

   tic

   Usinogram = zeros(Nxy, Nz, Mtheta);

   gammacur = gammavec(m);

   %choose LoRs falling into the neighborhood of current gamma

 gcurinds = (gammacoin > (gammacur - dgamma)) & (gammacoin < (gammacur + dgamma)); %gap width can be changed

   scurarr = scoin(gcurinds);

   vcurarr = vcoin(gcurinds);

   thetacurarr = thetacoin(gcurinds);

   gammacurarr = gammacoin(gcurinds);

   %add each coincidence to appropriate "slice"

   %!!! circular nature of theta currently ignored - may be improved

   for k = 1:sum(gcurinds)

     %closest subscripts

     ns = round((scurarr(k) + Lxy/2)/dr) + 1;

     nv = round((vcurarr(k) + Lz/2)/dr) + 1;

     ntheta = round((thetacurarr(k) + pi/2)/dtheta) + 1;

     %set lower and upper index limits for consideration of current LoR

     nsl = max(1, ns-20); nsr = min(Nxy, ns+20);
```

```
                nvl = max(1, nv-1); nvr = min(Nz, nv+1);
                nthetal = max(1, ntheta-1); nthetar = min(Mtheta, ntheta+1);
                %create current fragments of grid (should save time)
                sgrid = ((nsl:nsr) - 1)*dr - Lxy/2;
                vgrid = ((nvl:nvr) - 1)*dr - Lz/2;
                thetagrid = ((nthetal:nthetar) - 1)*dtheta - pi/2;
            [sgrid, vgrid, thetagrid] = ndgrid(sgrid, vgrid, thetagrid); %create 3D arrays
Usinogram(nsl:nsr, nvl:nvr, nthetal:nthetar) = Usinogram(nsl:nsr, nvl:nvr,
nthetal:nthetar) + ...
sinc((scurarr(k) - sgrid)/dr) .* sinc((vcurarr(k) - vgrid)/dr) .* sinc((thetacurarr(k) -
thetagrid)/dtheta);
                end
 save(['Sinograms/Sinogram' fileid '_incline' num2str(m) '.mat'], 'Usinogram');
                toc
            end
        end
        %SINOGRAMS PROCESSING
        if process_sinogram_flag
        Uimagefft_total = zeros(Nxy, Nxy, Nz); %array for the FT (uniform grid) of
the image
 %spatial frequencies of FFT outputs (theta = gamma = 0):
            ky0vec = 1/dr * (-Nxy/2 : Nxy/2-1)'/Nxy;
            kz0vec = 1/dr * (-Nz/2 : Nz/2-1)'/Nz;
            [ky0matr, kz0matr] = ndgrid(ky0vec, kz0vec);
            kx0matr = zeros(Nxy,Nz);
            %pitches of uniform grid:
            dkxy = 1/Lxy;
            dkz = 1/Lz;
            %coordinate arrays of uniform grid
            [kXuni, kYuni, kZuni] = ndgrid(ky0vec, ky0vec, kz0vec);
            %index vectors for decimation
            decindvecS = Pdecim * (0 : Nxy/Pdecim-1);
            decindvecV = Pdecim * (0 : Nz/Pdecim-1);
```

```
for mg = 1:Mgamma
    [mg Mgamma]
  gammacur = gammavec(mg);
load(['Sinograms/Sinogram' fileid '_incline' num2str(mg) '.mat']); %load appropriate array Usinogram
  Uimagefft = zeros(Nxy, Nxy, Nz); %array for the partial FT of the image
   %figure %debug
  tic
  for mt = 1:Mtheta %resample slice-by-slice
      %[mt Mtheta]
   thetacur = thetavec(mt);
  Usliceshift = fftshift(Usinogram(:,:,mt));
  Uslicefft = fft2(Usliceshift); %FFT along s- and v-dim.
Uslicefft = fftshift(Uslicefft); %move zero-frequency sample to the middle
  %compute locations of the NU grid points
  [kxmatr, kzmatr] = RotateByAngle(kx0matr, kz0matr, gammacur);
  [kxmatr, kymatr] = RotateByAngle(kxmatr, ky0matr, thetacur);
  %correct increasing samples density at the central part:
Uslicefft = Uslicefft .* sqrt(kxmatr.^2 + kymatr.^2) * dr; %rough compensation, range of gamma assumed small
    %DEBUG
%       subplot(121)
%       imagesc([-Lxy/2, Lxy/2-dr], [-Lz/2, Lz/2-dr], Usinogram(:,:,mt)')
%       subplot(222)
%       mesh(real(Uslicefft)); grid on
%       axis([0 Nz 0 Nxy -10 10])
%       subplot(224)
%       mesh(imag(Uslicefft)); grid on
%       axis([0 Nz 0 Nxy -10 10])
%       drawnow
  %find the closest points of the uniform grid
  %we assume that uniform nodes span from -0.5/dr to (0.5/dr - dk)
  %tic
```

```
                for ps = 1:Pdecim
                    for pv = 1:Pdecim
                        %take "decimated slice":
                        Uslicedecim = Uslicefft(ps + decindvecS, pv + decindvecV);
                        kxmatrdecim = kxmatr(ps + decindvecS, pv + decindvecV);
                        kymatrdecim = kymatr(ps + decindvecS, pv + decindvecV);
                        kzmatrdecim = kzmatr(ps + decindvecS, pv + decindvecV);
                        %find subscripts of the closest points
                        nxmatr0 = round((kxmatrdecim + 0.5/dr) / dkxy) + 1;
                        nymatr0 = round((kymatrdecim + 0.5/dr) / dkxy) + 1;
                        nzmatr0 = round((kzmatrdecim + 0.5/dr) / dkz) + 1;
                        %update unifrom saples at the closest and nearby points
                        for jxshift = -Jhalf:Jhalf
                            for jyshift = -Jhalf:Jhalf
                                for jzshift = -Jhalf:Jhalf
nxmatr = nxmatr0 + jxshift; nymatr = nymatr0 + jyshift; nzmatr = nzmatr0 + jzshift;
                        %confine ranges to avoid addressing errors
          nxmatr = max(1, min(Nxy, nxmatr)); nymatr = max(1, min(Nxy, nymatr));
nzmatr = max(1, min(Nz, nzmatr));
indmatr = sub2ind([Nxy Nxy Nz], nxmatr, nymatr, nzmatr); %matrix of "throughout"
indices
kXunicur = kXuni(indmatr); kYunicur = kYuni(indmatr); kZunicur = kZuni(indmatr);
%take appropriate node coordinates
Uimagefft(indmatr) = Uimagefft(indmatr) + Uslicedecim .* ...
sinc((kxmatrdecim-kXunicur)/dkxy) .* sinc((kymatrdecim-kYunicur)/dkxy) .*
sinc((kzmatrdecim-kZunicur)/dkz);
                                end
                            end
                        end
                    end
                end
                %toc
                %debug
```

```
                %mesh(kxmatr, kymatr, kzmatr); grid on
                %xlabel('kx'); ylabel('ky'); zlabel('kz')
                %axis(0.5/dr * [-1 1 -1 1 -1 1])
               %drawnow
              end
              toc
        save(['SliceFFTprojections/Resampled' fileid '_incline' num2str(mg) '.mat'], 'Uimagefft');
Uimagefft_total = Uimagefft_total + Uimagefft; %add resampled data to the final image FT
end
end
save(['ImagingResults/ImagingResults_' fileid '.mat']);
```